HEAT TRANSFER AND FLOW ANALYSIS OF A NOVEL LOW FLOW PIEZOELECTRIC AIR PUMP

by

Andrew S. Eastman

BS in Mechanical Engineering, Seattle University, 2007

Submitted to the Graduate Faculty of the

Swanson School of Engineering in partial fulfillment

of the requirements for the degree of

Master of Science

University of Pittsburgh

2013

UNIVERSITY OF PITTSBURGH

SWANSON SCHOOL OF ENGINEERING

This thesis was presented

by

Andrew S. Eastman

It was defended on

March 27, 2013

and approved by

Laura A. Schaefer, PhD, Associate Professor, Department of Mechanical Engineering and Materials Science

Anirban Jana, PhD, Senior Scientific Specialist, Pittsburgh Supercomputing Center, Carnegie Mellon University

Thesis Advisor: Mark L. Kimber, PhD, Assistant Professor, Department of Mechanical Engineering and Materials Science

HEAT TRANSFER AND FLOW ANALYSIS OF A NOVEL LOW FLOW PIEZOELECTRIC AIR PUMP

Andrew S. Eastman, M.S.

University of Pittsburgh, 2013

With the propagation of ever faster and more powerful electronics, the need for active, low power cooling is becoming increasingly apparent. In particular, applications which have traditionally relied only on natural convection will soon require an active cooling solution due to continually rising heat loads. A promising solution lies in utilizing piezoelectric materials via fans or pumps. Examples of such devices include synthetic jets and piezoelectric pumps, both of which rely on an oscillating diaphragm to induce flow. The device investigated in this thesis is able to generate flow rates up to 1 L/min and overcome pressures of over 2 kPa. The focus is to experimentally characterize the cooling potential of a piezoelectric-based air pump oriented normal to a heated surface, an environment similar to jet impingement. Experimental characterizations were made through the use of a thin film heater which provided a constant heat flux while an infrared camera was used to capture the resulting temperature field of the heated surface. Full-field data of the convection coefficient was analyzed as a function of vibration amplitude of the piezoelectric diaphragm and distance from the nozzle to the heated target. The maximum heat transfer coefficient was found to always be at the stagnation point regardless of vibration amplitude or distance to the target. Correlations have been developed which account for both variables considered and can be used to predict the performance of future designs which

rely on the same physical characteristics. Further, because of the piezoelectric blower's ability to overcome large pressure drops, a theoretical analysis was conducted to assess the viability of using them in oscillating flow cooling. It was found to be a reasonable driver of reciprocating flow that can keep fluid temperature change low. Additionally it was found that reciprocating flow allows for a more uniform temperature distribution over a heated surface.

TABLE OF CONTENTS

LIST OF TABLES

LIST OF FIGURES

NOMENCLATURE

English

A	Surface area of the thin plate
A_{ch}	Channel cross sectional area
A_p	Surface area of a single pixel
C	Specific heat
D	Nozzle diameter
H	Distance from the blower to the thin plate
Gr	Grashof number
h_{fc}	Forced convection heat transfer coefficient
$h_{fc,bar}$	Area-averaged forced convection heat transfer coefficient
h_{nc}	Natural convection heat transfer coefficient
I_s	Source current
I_b	Current to the blower
k_a	Thermal conductivity of air
k_f	Thermal conductivity of the fluid
k	Conduction heat transfer coefficient
L	Length of the thin plate
L_m	Length of the microchannel
Nu	Local forced convection Nusselt number

Nu_o	Stagnation forced convection Nusselt number
Nu_{bar}	Area-averaged forced convection Nusselt number
P_b	Power to the blower
P_{ch}	Perimeter of the channel
Pr	Prandtl number
q''	Heat flux
Q	Total heat generation
Q_t	Local heat generation at each pixel
Q_c	Heat loss due to conduction
Q_r	Heat loss due to radiation
Q_{nc}	Heat loss due to natural convection
Q_{fc}	Heat loss due to forced convection
R	Radius of circular heat source
t	Time
t_u	Unheated time
T_∞	Ambient temperature
T_s	Local surface temperature
U	Flow velocity
v_o	Maximum channel flow velocity
V	Vibration amplitude of piezoelectric diaphragm
V_s	Source voltage
V_b	Voltage to the blower
$\dot{V}_o$	Volumetric flow rate

x_o	Initial fluid position

Greek

δ	Thickness of the thin plate
ε	Emissivity of the thin plate
μ	Dynamic viscosity of the liquid
v	Kinematic viscosity of the air
ω	Oscillation frequency of the blower
ω_f	Oscillation frequency of the liquid
σ	Stefan-Boltzmann constant
ρ_f	Density of liquid
θ	Phase difference between oscillating voltage and current to the blower

ACKNOWLEDGEMENTS

The author wishes to thank Murata Manufacturing Co. Ltd. for funding this experimental research and providing the necessary materials to make this successful.

1.0 INTRODUCTION

Piezoelectric materials have been widely researched as a low power solution for fluid actuation. Applications range from intravenous introduction of pharmaceutical drugs [1] to bionic underwater propulsion [2]. The device configuration most common to these applications is a piezoelectrically actuated diaphragm. By itself, a single vibrating diaphragm produces no net flow (velocities are directed away from the diaphragm during half the stroke and then toward the diaphragm during the second half of the stroke). Therefore, multiple solutions exist to generate a positive net flow through either mechanical [2] or geometrical [3-7] regulation. The benefits of geometrically regulated pumps include ease of manufacturability and low power consumption while one of the main drawbacks is a decrease in net flow due to the backflow induced during the second half of the oscillation cycle. Synthetic jets [8-12] are another type of flow generation using an oscillating diaphragm. The largest difference between these devices and piezoelectric pumps is that, for synthetic jets (Figure 1), the inlet and outlet are the same opening. Thus, for half of the diaphragm vibration cycle, flow is entering the synthetic jet cavity and for the other half of the vibration cycle, flow is exiting. This means that the net mass flux through the orifice over one period of oscillation is zero. The blower that is investigated in this paper has a separate inlet and outlet and creates a net mass flux through its orifice putting it more in line with a standard piezoelectric pump. It does, however, exhibit some traits inherent in synthetic jets as well.

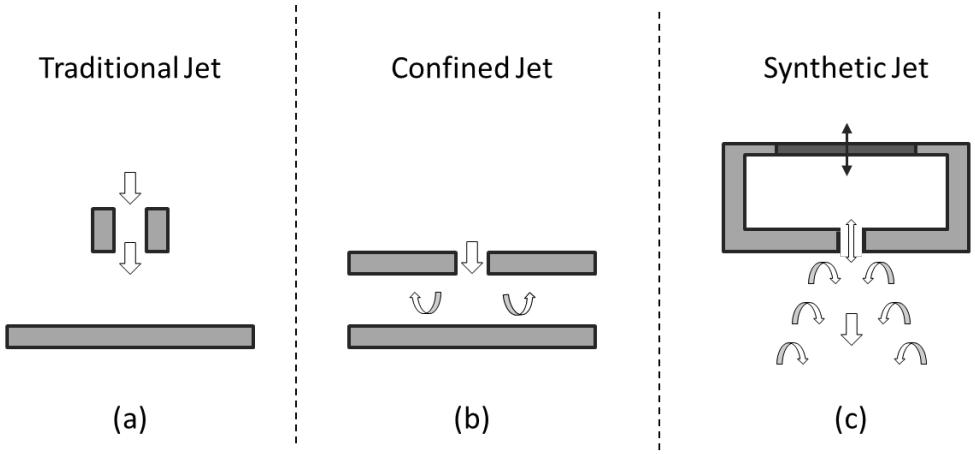

Figure 1: An illustration of the three types of jets referenced in this thesis. (a) traditional jet, (b) confined jet, and (c) synthetic jet.

Cheng et al. [2] used two independently operated magnetic coils to open and close the inlet and outlet. The objective was to look at utilizing the reversibility of the pumping mechanism in a piezoelectric pump in an underwater propulsion unit. It was theorized that this would allow for forward and backward motion without any need for a change in the overall structure in the pump. They developed a water resistant pump consisting of two chambers each fitted with a piezoelectric disk and operating in the first mode of vibration. The maximum displacement of the disk was found to be 28.8 μm. Operating at a frequency of 30 Hz with each coil open for half of the stroke, the maximum flow reached 164 mL/min. It was found that there was no discernible difference between the forward and reverse flow rate.

Although it is useful in limited situations, mechanical valve manufacturing inevitably becomes complicated as dimensions decrease. This issue can be alleviated with geometric regulation of flow direction. This is accomplished with an inlet and outlet diffuser design where one end of the valve is smaller than the other. A tapered hole encourages unidirectional flow towards the smaller opening. This is due to a higher back pressure to overcome in the opposite

direction. However, as the inlet and outlet are no longer mechanically opened and closed, they cannot completely eliminate backflow. Nonetheless, at such small sizes, machinability usually outweighs the inherent drawbacks for most applications.

A reciprocating micropump utilizing pyramid shaped flow channels was proposed and tested by Gerlach et al. [3, 4]. At 8 kHz, the pump was found to produce a flow of 480 μL/min. With pump dimensions of 10 mm by 10 mm, this flow rate was an order of magnitude higher than that of similar micropumps. This was at the high end of its output however, as the geometry limits operating frequency to between 100 Hz and 10 kHz. At the highest flow rates, the authors found the difference between the positive and negative flow rate directions to be 10 - 20% in favor of the positive direction. It is assumed that a larger difference between positive and negative flow would yield a higher flow rate. The low percentage difference indicates that there is considerable backflow in this micropump. At best, 80% of the potential flow is being lost by being drawn back in during the relief stroke of the piezoelectric element.

A model of the pressure vs. flow characteristics of valveless piezoelectric liquid pumps was developed by Olsson et al. [5] using a lumped mass model. It was found that vaporization of the fluid could occur within the pump chamber if the excitation of the piezoelectric was too high, thus creating a physical limiting factor due to low pressures. As expected, vibration amplitude was found to play a large role in flow rate and pressure. Their model also shows that the dimensions of the diffuser nozzles are integral for maximizing efficiency.

In order to understand how to enhance performance, Ulmann [6] attempted to analyze a single and double chamber valve-less piezoelectric pump. An equation for each pump configuration was found to be useful in calibrating design parameters based on nozzle diameter, operating frequency and displacement amplitude for a desired volumetric flow rate. It was found

that, in general, a smaller nozzle diameter is more likely to yield higher pressure capabilities. However, there is a limit to how small the nozzle diameter can be (less than 0.1 mm) before negative pressure is created within the pump chamber, negatively affecting performance. A double chamber pump yields a significant improvement over its single chamber counterpart. There is little difference between the two, however, when the single chamber is enlarged and a second piezoelectric element is applied. This insinuates that the number of chambers is not the main driving factor in piezoelectric pump performance. It is more likely that the overall volume displacement caused by the piezoelectric actuators themselves is a main determining factor in pump performance.

The dual chamber piezoelectric pump was also analyzed by Olsson at al. [7] to determine pressure and flow rate capabilities. The two pumps were arranged in a parallel configuration and the piezoelectric patch was operated with either in-phase or counter-phase excitation. Pump performance was found to be better with counter-phase operation. Despite only 20% of the fluid being brought in by the supply stroke, the maximum pump flow achieved was 16 mL/min and pressure was 16.7 kPa.

Synthetic jets (see Smith and Glezer [8] for an excellent review article on this topic) also share some commonality with the blower being investigated in this paper. Synthetic jets are composed of a piezoelectric element with only a single orifice that acts as an inlet and exit. When the piezoelectric patch is oscillated, it generates vortices that develop and detach downstream from their point of origin. By the time of the inlet stroke, the vortex is sufficiently far enough away to no longer be influenced by the inward flowing air. This vortex shedding creates flow in the desired direction without a mass flux through the jet itself. The lack of a mass

flux through the system makes it a poor pump, but it has uses in mixing and flow disruption technologies that make it a worthwhile research investment.

Chaudhari et al. [10] investigated impingement cooling of an axisymmetric synthetic jet for a fixed heater size and varying orifice diameters. The Reynolds number ranges from 1150 to 4180 and the oscillation frequency varies from 100 to 350 Hz. The setup consisted of a copper plate affixed to a heater which was surrounded by insulating materials. The copper plate had two thermocouples placed 4 mm below the lateral surface on opposite sides to gather an average temperature.

Valiorgue et al. [12] investigated both the heat transfer capabilities and flow field of a synthetic jet. They investigated a Reynolds number range of 1000 to 4300. The experimental setup was similar to that presented in this paper with the exception of certain essential changes to allow for Particle Image Velocimetry measurements. They found that there is a critical stroke length where two flow regimes meet. A correlation was also developed, however it was only based on stroke length which was not one of the parameters considered in this paper. Therefore it was not used as a comparison.

The piezoelectric pump studied in this paper consists of a single outlet nozzle with a large inlet. Its unique construction allows it to overcome pressures over 2 kPa as well as promoting better manufacturability. Additionally, the pump has been recorded as yielding a flow rate of over 1 L/min. The large potential operating pressure allows for use in applications where low flow and high pressure is important (e.g., microchannel applications). The flow rate is notable in that it is at least one order of magnitude higher than pumps of similar dimensions [2, 7]. Notable dimensions of the blower are that the piezoelectric element is roughly 15 mm in diameter, nozzle diameter (D) is 1 mm and the total housing footprint is 20 mm square. All of this is

accomplished with minimal, if any, back flow. The typical Reynolds number range encountered with this blower is 500-650.

As the impingement orientation is of primary importance in this work, it is important to compare our results with those traditionally accepted for jet impingement. Many correlations have been developed to characterize jet impingement heat transfer using air as the working fluid. One of the first proposed is that from Martin [13], which is based on several sets of experiments. Based on the applicable Reynolds number range of this correlation, it is evident that turbulent jets are of primary significance ($2000 \leq Re \leq 400000$). In addition, the valid range in the domain size of the heated surface ($2.5 \leq R/D \leq 7.5$) and distance from nozzle to heated surface ($2 \leq H/D \leq 12$) is also limiting, especially when considering small jet nozzles as is the case in the current study.

Goldstein et al. [14] developed a correlation that encompassed a larger domain size of the heated surface ($0.5 \leq R/D \leq 32$), but only looked at very large Reynolds numbers ($61000 \leq Re \leq 124000$). Attempting to develop a correlation following the work of Martin [13], Huang and El-Genk [15] also included the stagnation point in their correlation. However, as with the previous correlations, the range of validity was very limited ($6000 \leq Re \leq 60000$, $0 \leq R/D \leq 10$, $1 \leq D \leq 12$). Of the studies found, Tawfek [16] developed correlations valid over the largest range ($3400 \leq Re \leq 41000$, $2 \leq R/D \leq 30$, $6 \leq D \leq 58$), yet the correlation is broken up into four separate, overlapping ranges. No area averaged correlation has, to the author's knowledge, been investigated for low Reynolds number continuous jet impingement flow. A recent study by Chiriac and Ortega [17] has focused on low Reynolds number heat transfer characteristics for slot jets developed a numerical model to predict the local and stagnation heat transfer based on the Reynolds number and slot width. However, no studies have been found relating to circular air

jets at low Reynolds numbers. Most of the correlations for synthetic jets have investigated low Reynolds numbers although the number is few. Of the correlations proposed for synthetic jets, only one by Persoons et al. [18] was deemed applicable as a comparison.

On the other hand, numerous high Reynolds number correlations exist for stagnation heat transfer performance in jet impingement. Huang and El-Genk [15] extended the range of validity from Goldstein et al. [14], including stagnation. Lytle and Webb [19] developed a correlation for a somewhat limited range of interest ($0.1 \leq D \leq 1$). An analytical correlation was derived by Kendoush [20] for the stagnation point. It claims to be verified at $D = 8$ and $D = 24$, but graphical examination of this correlation does not yield expected results and there is little documentation to further verify its validity. San and Shiao [21], Li and Garimella [22], Schroeder and Garimella [23] and many others [17, 24-26] have developed stagnation correlations for confined jet impingement. However, these studies focus on turbulent jets at relatively small distances from the heated surface. It was also found that confined jet impingement heat transfer cannot be effectively predicted by correlations for free jet impingement [27].

Another, less common, method of heat transfer is via an oscillating fluid. With this process, the reciprocating motion of the fluid results in zero net mass transfer over a cycle. This has some unique uses, particularly where the working fluid is expensive or there is no adequate means of fluid storage. Previous experimental work by Kurzweg [28] found that the conduction heat transfer rates were very large and exceeded that seen in current heat pipe technology. Zhao and Cheng [29] numerically determined that the Nusselt number in a pipe was a function of the kinetic Reynolds number, oscillation amplitude of the fluid, and ratio of the length and diameter of the pipe. This is contrary to the fact that under steady flow conditions the Nusselt number is

constant that only depends on the heating conditions. This was later verified experimentally by Akdag and Ozguc [30] with similar results. Due to the high pressure and flow rate capabilities of the piezoelectric blower, it would be worthwhile to investigate the feasibility of this type of application.

The purpose of this work is to analyze the thermal performance of low Reynolds number jet impingement where the net flow is provided from an oscillating piezoelectric diaphragm. Correlations were determined to estimate the most efficient placement and operation for a desired cooling effect. Both the area averaged and stagnation Nusselt numbers were of interest and compared to previous correlations for jet impingement heat transfer. Additionally, a theoretical examination of the cooling potential and temperature distributions under oscillating flow conditions is also conducted.

2.0 EXPERIMENTAL SETUP AND PROCEDURE

The Murata Manufacturing Company provided a piezoelectric blower that operates in a novel way. Although there is little that can be revealed about its specific construction or operational characteristics due to confidentiality, the goal was to determine the heat transfer capabilities under various conditions in order to get a better idea of how well it would work for electronics cooling. An impingement flow orientation was decided upon to be the first setting for which to conduct tests.

2.1 IMPINGEMENT HEAT TRANSFER SETUP

The uniform heat generating surface consisted of a thin stainless steel sheet (76.2 mm x 101.6 mm x 0.0508 mm). This sheet was soldered to two copper bars (76.2 mm x 25.4 mm x 12.7 mm) using a tin and lead based solder and a hot plate. As the stainless steel-copper interface covered 12.7 mm from both ends of the sheet, a surface area of 76.2 mm x 76.2 mm was left exposed to the air on both sides. The copper bars served as voltage terminals, and due to uniform heating within the stainless steel sheet, a constant heat flux was generated. Each copper bar was affixed to a block of Teflon (127 mm x 76.2 mm x 38.1 mm) to act as a thermal and electrical insulator. The Teflon blocks were affixed to two 12.7 mm diameter stainless steel rods with springs in between to create an opposing force. This allowed the stainless steel sheet to be kept under

tension and therefore flat through thermal expansion. This heater assembly was positioned such that the heated surface was in a vertical orientation. As Figure 2 illustrates, the blower is positioned on one side of the heated surface with an infrared camera (FLIR SC5000) on the opposite side in order to measure the temperature distribution. As the stainless steel sheet is very thin, the conduction through the thickness is negligible and the temperature contours are the same on either side. A laser displacement sensor (Keyence LK-H022) was mounted behind the blower to record the oscillatory displacement of the piezoelectric element in order to ultimately characterize the performance as a function of vibration amplitude. The stainless steel was coated on both sides with a thin layer of Krylon 1602 Ultra Flat black spray paint. This paint has a known emissivity of 0.95 [31] and therefore allows the surface temperatures to be quantified via infrared thermometry.

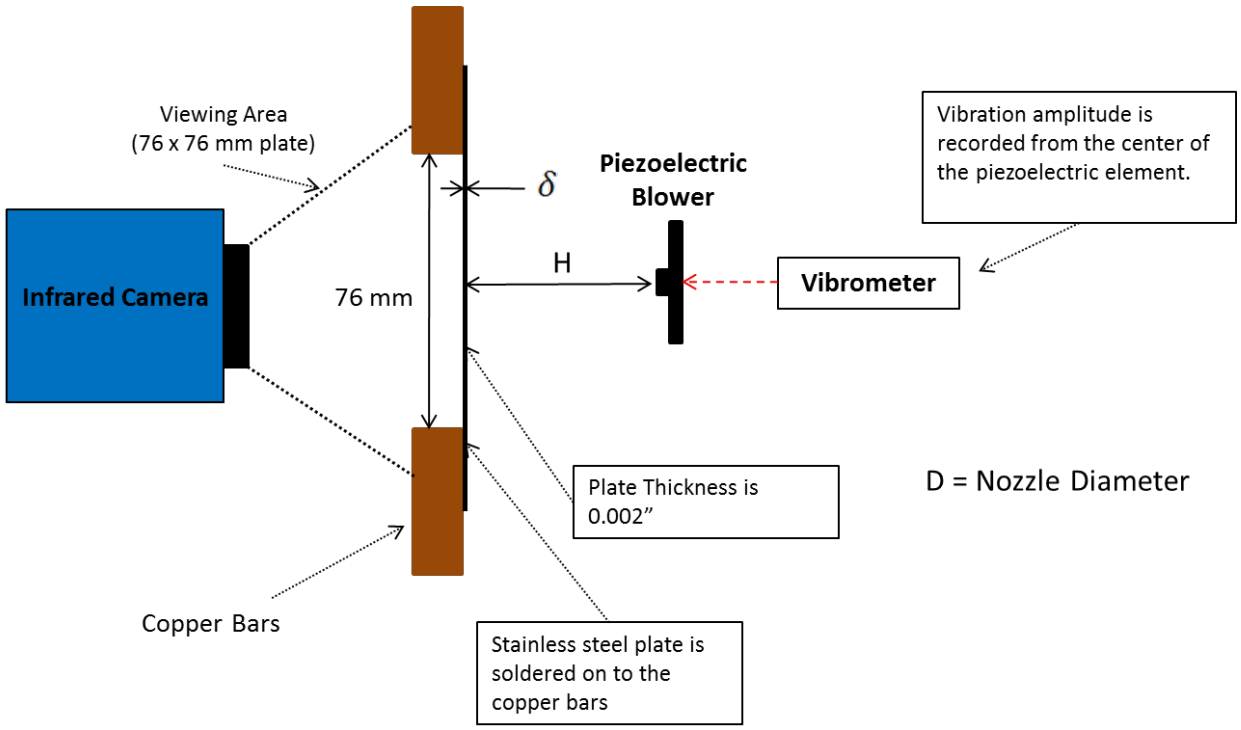

Figure 2: Diagram of how the components of the test are oriented.

The thin plate was heated using a high current DC power supply (TDK-Lambda Zup 10-40). Two contacts were made to the copper bars on both sides of the plate (seen in Figure 3). The source voltage (V_s) was recorded across the thin plate where the wires meet the copper bar. Current across the plate (I_s) was measured using a current shunt that was placed on the positive side of the circuit. The total generated heat (Q) can then be determined according to:

$$Q = V_S I_S \tag{2.1}$$

The blower was powered by a function generator (Tektronics AFG 3102) to allow for control of the oscillation frequency and input voltage amplitude of the piezoelectric patch. In order to determine the power consumption of the blower, a resistor was used as a shunt to measure the current input to the blower (I_b) via a measurement of the voltage drop across the resistor. Thus, the power consumption can be quantified according to [32]:

$$P_b = V_b I_b \cos(\theta) \tag{2.2}$$

where V_b is the voltage across the two leads of the blower (after the initial voltage drop across the resistor) and θ is the phase difference between the voltage and current signals.

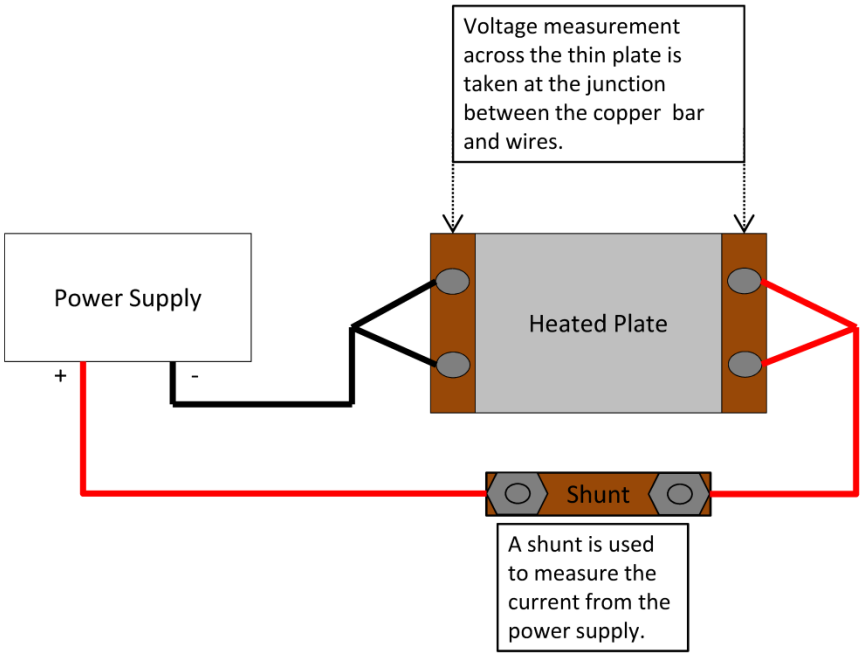

Figure 3: Wiring diagram of the heated thin plate.

The infrared camera, blower, heater assembly and laser displacement sensor were all mounted within a 0.61 m by 0.61 m by 1.22 m enclosure made of clear plexiglass. The blower, heater assembly and laser displacement sensor were mounted on linear stages to ensure repeatability and precise control of reference distances. The enclosure is designed to allow operation of all equipment inside without removal of any of the side walls or the top panel. Three holes at the bottom of the front panel allow for operation of the equipment (e.g. changing distance between the blower and heated surface) without measurably affecting the integrity of the experiment. This enables a more consistent steady state temperature due to isolation from external flows within the laboratory.

Four thermocouples mounted at various locations throughout the enclosure were used to quantify the ambient temperature. As shown in Figure 4, the locations were: 1) slightly below the

thin film for the air that is brought in by natural convection (position *1*), 2) at the blower inlet for the air being blown onto the plate surface (position *2*), 3) on the table surface (position *3*), and 4) in the air near the center of the enclosure but with careful attention to not place it above any heat producing equipment (position *4*). An ice point reference (Omega TRCIII) was used to give a uniform near zero reference temperature and thus increase thermocouple accuracy. As the forced convection from the blower is of primary importance in this work, the ambient temperature used in calculating convection coefficients is that of the temperature of the blower inlet.

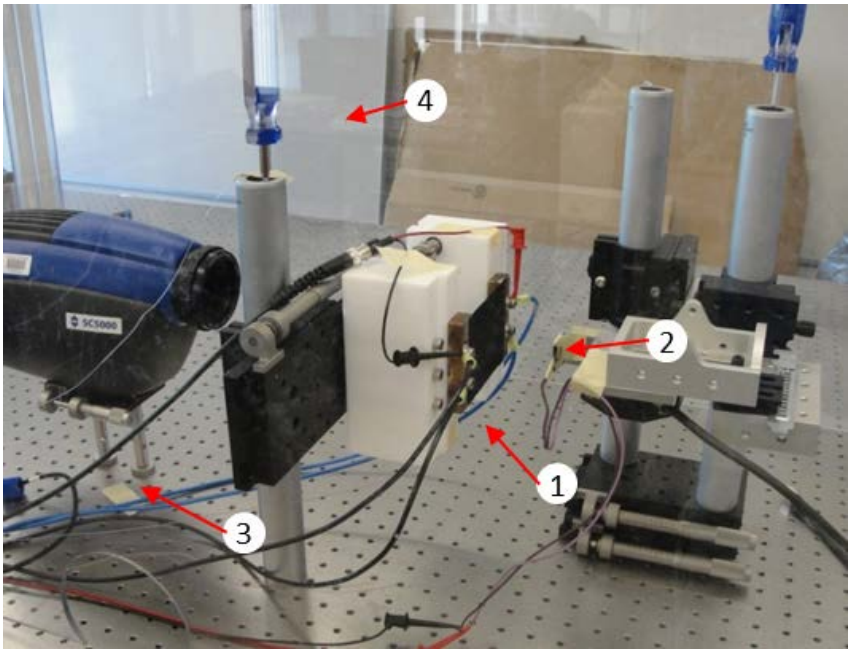

Figure 4: Picture of the test setup where the location of each thermocouple is marked with a colored dot.

Table 1 gives some important operational attributes of the blower at the 7, 8 and 9 V inputs. The source voltage is recorded based on the output settings of the function generator. The vibration amplitude was found to change very slightly with an increased voltage input. As a result, the effect on the distribution of convection coefficient is minimal as well. The power requirement of the blower is in the range of 80 to 100 mW.

Table 1: Important operational attributes of the blower at different voltage inputs.

Function Generator Setting (V)	7.0	8.0	9.0
Vibration Amplitude (μm)	5.0	5.3	5.5

2.2 PROCEDURE

The blower was mounted on an aluminum beam that allowed only the blower to operate near the thin plate. The orientation was such that the inlet of the blower was fully exposed while the outlet was given a hole in the aluminum beam through which to operate. The depth of the hole was such that the end of the nozzle was flush with the side closest to the thin plate. The aluminum was formed in an "S" shape where a surface area not much larger than the blower would touch the thin plate if the nozzle to plate spacing (H) was ever lowered to zero. This was to reduce interaction of the thin plate with anything other than the flow generated by the blower. The entire system was elevated 76 mm above the mounting table to reduce boundary effects. The power supplied to the thin plate was set such that the minimum temperature observed across all experiments never dropped below 40°C, which would provide a temperature difference between the ambient of 10-15°C. A temperature difference of this magnitude was important to ensure low uncertainty in convection coefficients.

The procedure followed for any given set of experiments began by turning on the power supply, and allowing the enclosure to reach steady state temperatures. The table surface temperature does not quite reach steady state due to the added thermal mass of the table itself. However, as the three other thermocouples indicate the ambient air reaching steady state and the table surface temperature having very limited effect on the heated plate, there was little reason to prolong the wait. This was typically achieved after approximately 2.5 hours. The time history of

the four thermocouple readings during this interval is shown in Figure 5. The variable parameters of interest in this work are the vibration amplitude of the diaphragm (V) and the distance from the blower to the heated surface (H). Tests were conducted at 7, 8 and 9 volt outputs from the function generator which corresponds to 5.0, 5.3 and 5.5 μm for the vibration amplitude levels. Measurements were taken from a distance (H) of 1 mm to 59 mm in 2 mm increments. Each thermal image analyzed represents an average of nine separate sets of data captured by the infrared camera in one second intervals.

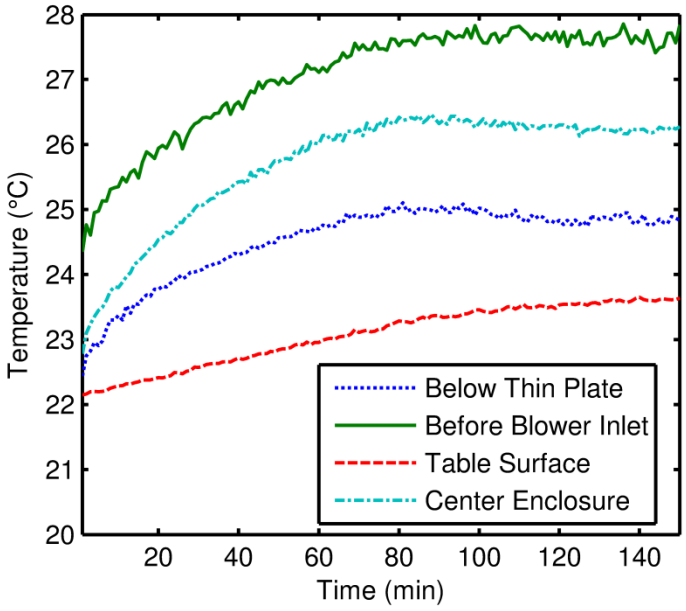

Figure 5: Graph of the temperature in the enclosure reaching steady state.

The heat balance for a small volume of the heated surface (e.g., a single pixel from the infrared camera imaging plane) reveals the expressions needed to compute the convection coefficients. The generated heat (Q_t), which is dependent on the total heat (Q), the pixel area (A_p), and the total area (A), is dissipated through radiation (Q_r), lateral conduction (Q_c), and both natural (Q_{nc}) and forced (Q_{fc}) convection according to:

$$Q_t = \frac{QA_p}{A} \tag{2.3}$$

$$Q_t = Q_r + Q_{fc} + Q_{nc} + Q_c \tag{2.4}$$

The heat loss due to conduction is potentially significant depending on its relative magnitude compared to the total heat generation and thus is an important part of our analysis. The pixel to pixel conduction losses were analyzed according to:

$$Q_c = k\delta\left(T_{m+1,n} + T_{m-1,n} + T_{m,n+1} + T_{m,n-1} - 4T_{m,n}\right) \tag{2.5}$$

where *m* and *n* are the pixel indices, *k* is the plate thermal conductivity, δ is the plate thickness, and *T* the temperature of the plate at each pixel based on *m* and *n*. Therefore the lateral conduction losses are dependent on the temperatures of the neighboring pixels (i.e., lateral conduction would be zero for a uniform temperature profile). The magnitude of the temperature gradients on the surface (i.e., between neighboring pixels) are what ultimately determines the magnitude of the lateral conduction losses. Utilizing Eq. (2.5) also allows for accounting for heat loss along the edges near the copper bars. Edge heat loss would additionally only really be a concern when the effect of the blower convection is near the edge.

In order to quantify the natural convection heat transfer coefficient, the following correlation was used for a vertically oriented flat surface [33]:

$$h_{nc} = \left(\frac{4}{3}\right)\left(\frac{k}{L}\right)\left(\frac{Gr}{4}\right)^{1/4} g\left(\mathrm{Pr}\right) \tag{2.6}$$

Where *Gr* is the Grashof number, h_{nc} is the natural convection heat transfer coefficient, *L* is the length of the plate, and *g(Pr)* is a function defined in [33] based on the Prandtl number. To confirm the accuracy of Eq. (2.6), tests were run with the heater under natural convection conditions (no forced convection from the blower). The experimental results were compared to Eq. (2.6) at the same average plate temperature. Figure 6 illustrates the temperature profile of the

thin plate under no forced convection. The surface behaves as expected for a vertically oriented surface when subjected to a constant heat flux with natural convection. The temperature is the lowest at the bottom of the plate and increases according to a $1/5^{th}$ power law [33].

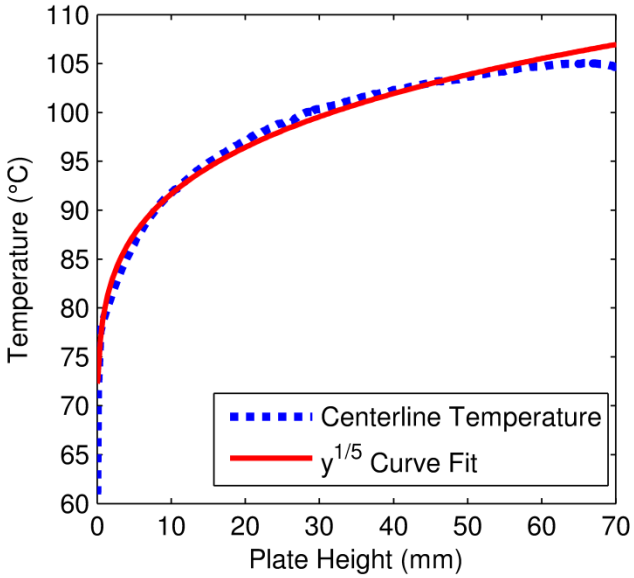

Figure 6: Vertical temperature profile of the thin plate under natural convection conditions.

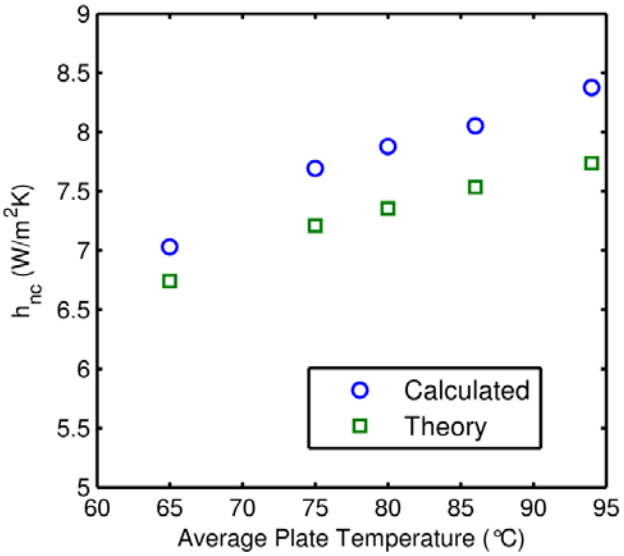

Figure 7: Comparison of the calculated natural convection heat transfer coefficient with two separate theoretical calculations. The theory is from Eq. (2.6).

With the thin plate at different average surface temperatures, the natural convection heat transfer coefficient was calculated. Comparison of the theoretical value to the calculated value, shown in Figure 7, reveals that they are within 10% of each other. This does show that the theory that is used under-predicts the actual natural convection heat transfer coefficient, but the overall influence of the natural convection coefficient plays a small enough role that a 10% error is less than a percentage point overall.

If the assumption is made that ambient and surrounding temperatures are equal (although the two temperatures are slightly different the resulting change in radiative heat transfer is negligible), Eq. (2.4) can be solved to ultimately determine the forced convection heat transfer coefficient (h_{fc}):

$$h_{fc} = \frac{\left(\frac{Q_t - Q_c}{A_p} - 2\varepsilon\sigma\left(T_s^4 - T_\infty^4\right) \right)}{\left(T_s - T_\infty\right)} - h_{nc} \tag{2.7}$$

where ε is the emissivity [31] of the painted plate, σ is the Stephan-Boltzmann constant, T_s is the surface temperature of the plate and T_∞ is the ambient temperature.

2.3 UNCERTAINTY ANALYSIS

Every variable that contributed to determining the heat transfer coefficient was measured directly in order for application of a complete analysis of uncertainty. All uncertainty analysis was done using a simple t-test with a 95% confidence interval. Precision error was also included.

The surface temperature of the thin sheet was determined using an infrared camera with a precision uncertainty of 1°C. The infrared camera was factory calibrated, however the calibration was verified using a blackbody system (Infrared Systems Development IR-2106/301). Each thermal image consisted of nine temperature captures at each distance (*H*). The ambient temperature is measured via thermocouples with an uncertainty of 0.5°C. Therefore, the uncertainty in the difference between surface and ambient temperatures is 1.17°C. This yields an uncertainty of approximately 4% to 4.5% at the stagnation point. The ambient temperature was calculated from 120 data points in one second intervals with a thermocouple data acquisition unit (NI-9211). This yields a precision uncertainty of 0.015%.

The measurement of voltage and current to the thin plate were both taken with a data acquisition unit (Measurement Computing USB-1608HS) for 200 data captures. The precision error was calculated, based on the rated resolution of the data acquisition unit, at 0.0015 V and 0.15 A. This yields a total voltage and current measurement accuracy of about 0.3% and 0.8% respectively. The uncertainty of the area measurement of the thin stainless steel sheet, consisting of only precision error, was calculated as 1.5%.

The total heat transfer convection coefficient accuracy was calculated by combining all of the above accuracy calculations, resulting in an experimental stagnation point uncertainty of approximately 7%. A more detailed explanation of the equations used and process can be found in Appendix B.

3.0 RESULTS AND DISCUSSION

The objective of the research included in this paper was to determine the experimental heat transfer coefficient and consequent Nusselt number produced by this piezoelectric blower under impingement cooling conditions. Then, in order to provide a basis for predicting the cooling performance under other conditions, a correlation was developed for both the stagnation point and area averaged Nusselt number. There was also a proof of concept analysis of the viability of using this blower under oscillating flow conditions. Accompanying this theoretical analysis is a brief discussion of the viability of not only the piezoelectric blower's application, but the utilization of the concept of reciprocating flow in general.

In Figure 8, the radial temperature (the temperature profile that originates at the stagnation point and travels in a straight line along the heated plate surface) profiles for different values of *H/D* can be seen. It is apparent that the closest distance (*H/D* = 5) experiences the largest temperature gradient compared to the other distances. Although not shown, this feature shows a gradual change from *H/D* = 5 to *H/D* = 15. This is mainly due to the area over which the flow occurs being very small when the nozzle is close to the heated surface. As was previously discussed, these higher temperature gradients cause lateral conduction effects to increase.

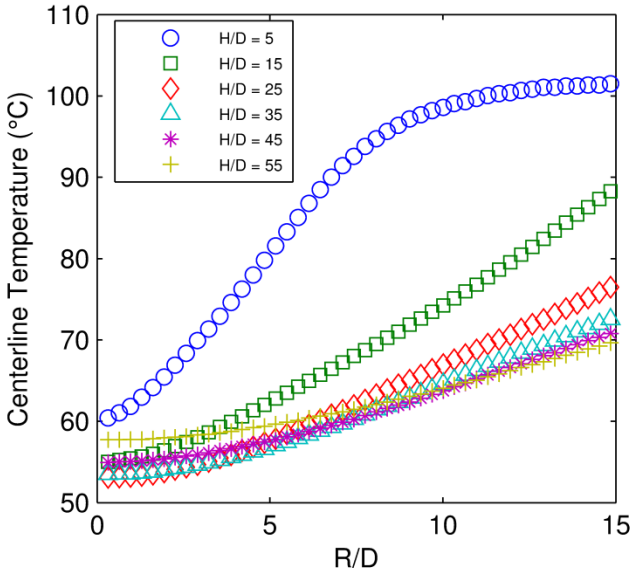

Figure 8: Radial temperature profiles at various distances for V_b = 8 V.

Neglecting or including lateral conduction can be significant as is shown in Figure 9. For small plate to blower spacing (*H*) and lateral conduction neglected, the experimental heat transfer coefficient is under predicted by a factor as high as 5. These temperature fields are used in Eq. (2.7) to determine the full field heat transfer coefficients. These values can then be analyzed further to determine the area-averaged convection coefficient ($h_{fc,bar}$) as a function of size of heated target. A circular geometry for the heater is assumed and the average thermal performance is quantified according to:

$$h_{fc,bar} = \frac{1}{R}\int_0^R r h_{fc} dr \tag{3.1}$$

where *R* is the radius of the inspected area of the plate.

A sample of the area-averaged heat transfer coefficient as a function of radius of heated surface can be seen in Figure 10. As would be expected, the blower produces heat transfer above what is seen from natural convection alone. At *H/D* = 5 a heat transfer coefficient of nearly 175

W/m^{2}K can be achieved. This is roughly 30 times larger than natural convection at that point (h_{nc} = 6 W/m^{2}K). Such a high stagnation heat transfer coefficient at a low H/D can be attributed to, as will be discussed later in this thesis, lateral conduction. Even at H/D = 55 the enhancement over natural convection is more than 10 times as high at the stagnation point. An important aspect to note, and which will be discussed further, is that as H/D increases, the peak seen in the area-averaged heat transfer coefficient becomes less pronounced. The convection coefficient (h_{fc}) was analyzed as a function of the vibration amplitude of the blower (V) and the distance from the nozzle to the heated surface (H). These three variables are expressed in dimensionless form through proper definitions of the Nusselt number (Nu), Reynolds number (Re), and dimensionless gap (H/D). The length scale used for each of these parameters is the nozzle diameter (D), a convention typically used in jet impingement studies [8-10, 13-16, 19, 21, 22, 24, 26, 27, 31]. The Nusselt and Reynolds numbers are defined according to:

$$\mathrm{Re} = \frac{UD}{\nu} \tag{3.2}$$

$$Nu = \frac{h_{fc} D}{k_a} \tag{3.3}$$

where ν is the kinematic viscosity, U is the fluid velocity, and k_a is the thermal conductivity of air taken as 1.86x10^{-5} m^2/s and 0.026 W/mK, respectively.

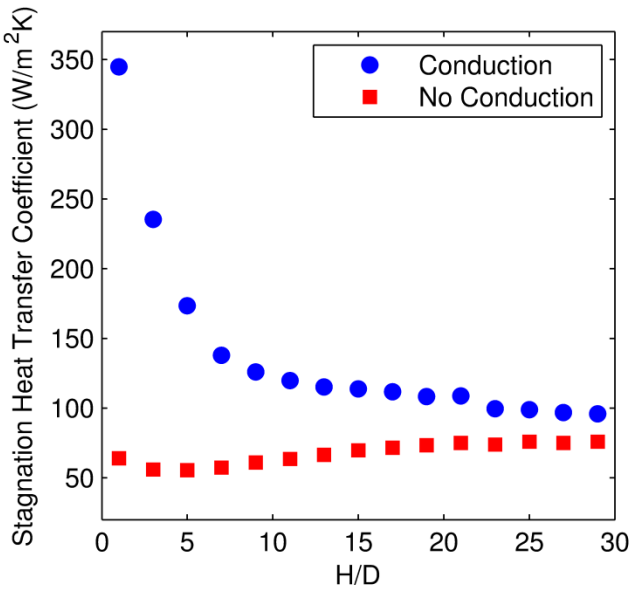

Figure 9: Comparison of the stagnation Nusselt number (V_b = 8 V) with and without lateral conduction.

The full-field Nusselt numbers are shown for *H/D* = 5 and *H/D* = 25 in Figure 11(a) and (b), respectively. As expected, the resulting contours reveal a circular cooling pattern at both distances. The overall heat transfer performance of the blower is much higher for *H/D* = 5 although the area of the blower's effectiveness is limited. In other words, one must allow for a reduction in the area of coverage for a higher localized thermal performance. For both cases, the highest heat transfer occurs at the stagnation point, a behavior consistent across all data captured in this study.

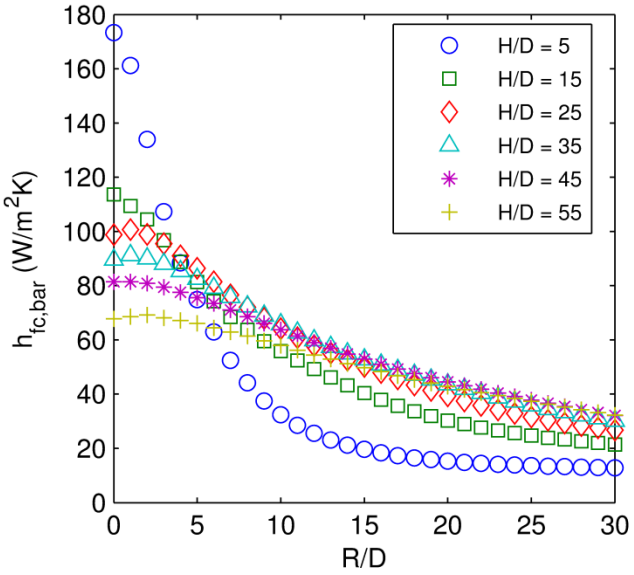

Figure 10: Area-averaged heat transfer coefficient for V_b = 8 V.

Similar experimental results were gathered from *H/D* = 1 to *H/D* = 59 and the profiles of each exhibited circular patterns of cooling. Attempts were made to develop empirical relationships to aid in predicting the thermal performance. In particular, both the stagnation point Nusselt Number (Nu_0) and the radial averaged Nusselt Number (Nu_{bar}) were analyzed. These quantities are defined according to Eq. (3.3) and calculated from the raw data according to Eqs. (3.4) and (3.5) for stagnation and area averaged values, respectively:

$$Nu_o = \frac{h_{fc}\left(x=0, y=0\right)D}{k_a} \tag{3.4}$$

$$Nu_{bar} = \frac{h_{fc,bar}D}{k_a} \tag{3.5}$$

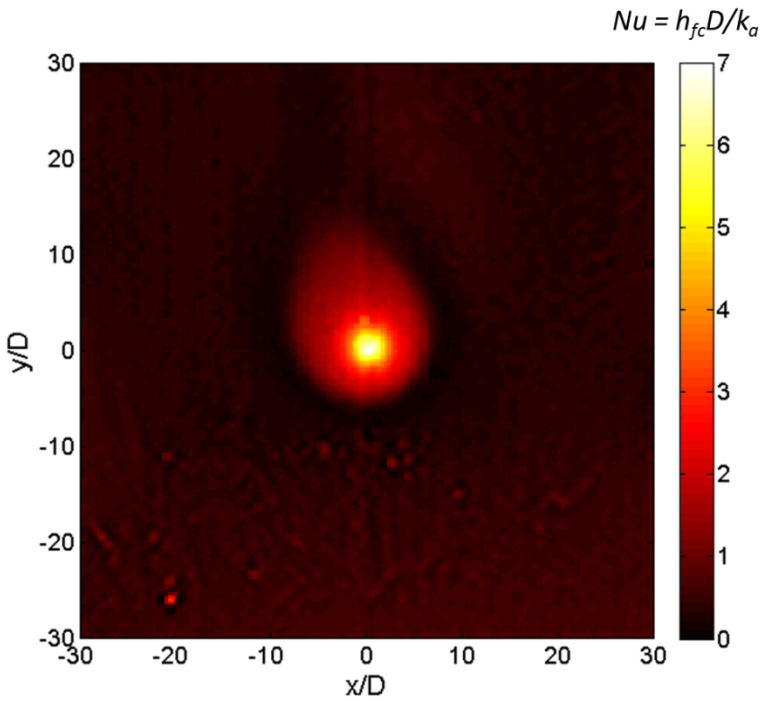

(a)

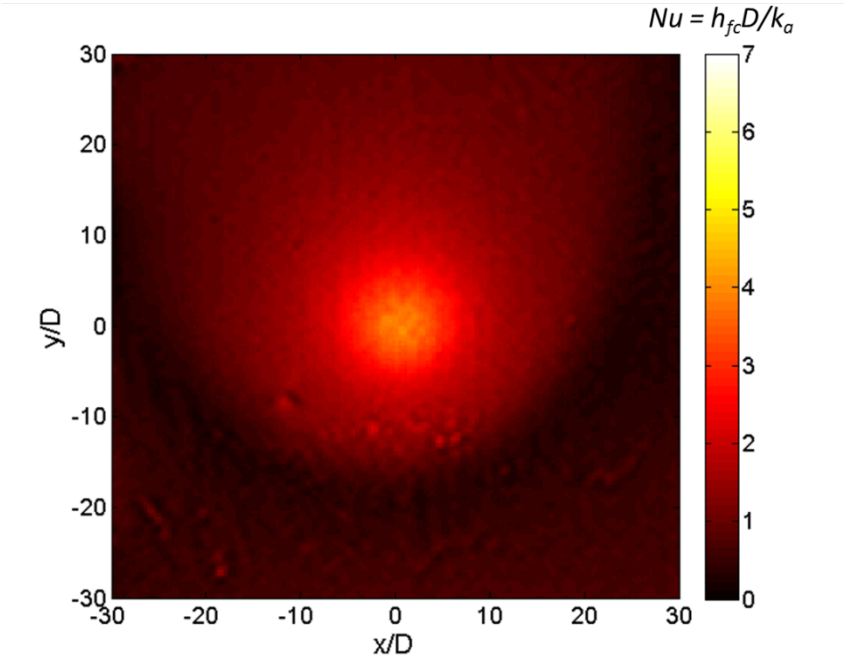

(b)

Figure 11: Nusselt number map of the thin plate when subjected to forced convection from the blower at (a) *H/D* = 5 and (b) *H/D* = 25.

To better understand the importance of Nu_{bar}, consider the situation where cooling is required for a set of heat sources of varying surface area. This area averaged value gives an idea of the total heat being removed over a given area. This allows for maximization of blower performance based on the size of the heat source.

3.1 STAGNATION HEAT TRANSFER

The thermal performance as a function of distance between the heated plate and blower (*H/D*) is displayed in Figure 12 for three different voltage inputs (V_b) (and therefore three separate vibration amplitudes). It is apparent that the trends are very similar with a voltage increase causing only a small shift in the Nusselt Number. The maximum stagnation Nusselt Number occurs when the blower is closest to the heated plate. This would not be evident unless lateral conduction is taken into account. For small plate to blower spacing, the cooling effect is very much localized, which in turn causes a very steep temperature gradient at the stagnation point. Large temperature gradients cause the lateral conduction, or thermal smearing, to be non-negligible. This effect is quantified and presented in more detail later in this paper (stagnation heat transfer discussion). It is important to note that for all three voltage inputs, the behavior is similar. In other words, the performance is maximized when the blower is closest to the heat source. This indicates that the optimal operating parameters do not change within our voltage input range (and therefore, vibration amplitude). The error bars shown at each data point were found from the previously mentioned detailed uncertainty analysis. It can also be gathered by this data that a reduction in voltage input (V_b) from 9 to 7 V would not drastically reduce

performance for *H/D* greater than 3. This means that similar performance can be realized even when the power input to the blower is reduced, which is very important from an energy management point of view. The following expression is proposed to capture the defining characteristics of each curve shown in Figure 12:

$$Nu_o = \left[A_1 e^{-\left(B_1 \frac{H}{D}\right)} + C_1 e^{-\left(E_1 \frac{H}{D}\right)} \right] \mathrm{Re}^{F_1} \tag{3.6}$$

Where *A*, *B*, *C*, *E* and *F* are constants whose optimum values are found from a least squares fit of the experimental data and the applicability ranges are $1 \leq {}^{H}/_{D} \leq 59$ and $550 \leq Re \leq 622$. The result of the best fit yields A_1 = 6.05, B_1 = 0.37, C_1 = 2.5, E_1 = 0.012 and F_1 = 0.120. This curve fit can now be used to predict the stagnation Nusselt Number (Nu_0) for a given Reynolds number and *H/D* of the blower. It can be seen that the dependence on Reynolds number, and consequently vibration amplitude, is limited in determining Nusselt number. Tests were performed with a flow meter (Omega FMA-A2107) on the blower and reveal the Reynolds numbers to be 557, 596 and 622 for V_b = 7, 8 and 9 volts respectively. The flow meter has an accuracy of +/- 0.02 L/min which corresponds to an uncertainty in the Reynolds number of 3.8%. The magnitude of this dimensionless parameter precludes the use of many conventional jet impingement correlations. However, comparisons are made with a few well accepted relationships in order to better understand their relation to our experimental trends.

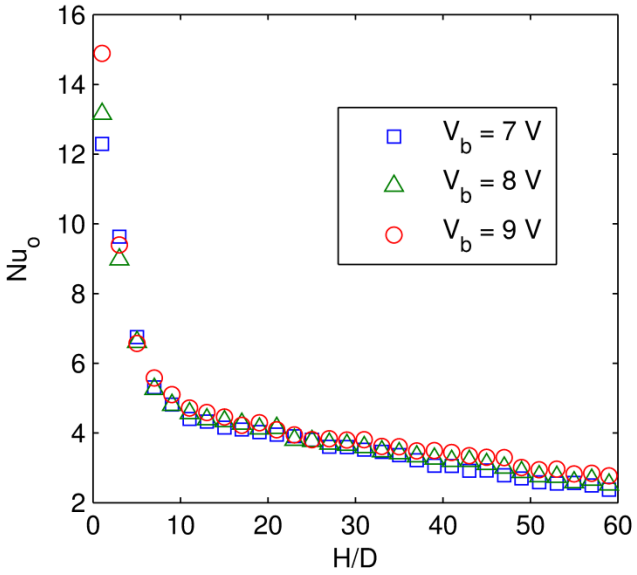

Figure 12: Stagnation Nusselt number for all three voltage inputs.

Figure 13 compares the developed stagnation correlation with those from Huang and El-Genk [15] ($6000 \leq Re \leq 60000$, $1 \leq H/D \leq 12$), Persoons et al. [18] ($500 \leq Re \leq 1500$, $2 \leq H/D \leq 16$) and Schroeder and Garimella [23] ($5000 \leq Re \leq 20000$, $0.5 \leq H/D \leq 4$) using $Re = 596$. These correlations consider air as the working fluid, but are focused on free and confined jets, respectively. The confined jet impingement correlation was chosen because it was felt that for small H/D, confined flow might be more appropriate. It is apparent that none are an ideal fit for the current data in the ranges depicted in the figure. Persoons et al. [18] does not exhibit the same magnitude in cooling effect as the others. As the presented correlation is more in line with those looking at continuous jet impingement, it gives the impression that the performance of the blower is more similar to a continuous jet rather than a synthetic jet. The Huang and El-Genk correlation more closely resembles our data for $H/D > 7$, but there is no good fit for small values of H/D (less than 2.5). In fact, it is stated in their paper that conduction was only considered to contribute 2% to heat loss and only through the mounting surface. Although Huang and El-Genk

[15] did not consider lateral conduction in their study, a brief analysis of their data suggests this could be significant, especially near the lower bounds of their Reynolds numbers. Looking at their data for H/D = 2 and Re = 46233, their heated surface temperature changes near the stagnation region by about 30 °C over a 5 mm distance. They have a heated surface with the same material properties and thickness as that used in this paper (k = 16 W/mK and δ = 0.0508 mm). If we consider the stagnation region to be a square which is 5 mm x 5 mm and the temperature increases in all directions away from this region by 30 °C over a distance of 5 mm, then the temperature gradients from four directions are all equal to 6 K/mm. The area for conduction will be 5 mm by 0.0508 mm. This yields a lateral conduction of nearly 0.1 W. The heat generated for this 5 mm x 5 mm stagnation area could be as high as 0.255 W based on the maximum report heat flux of 10.2 kW/m^2. Therefore, according to this analysis, the stagnation heat transfer coefficient in this case is under-predicted by roughly 40% as it is borrowing heat from neighboring pixels or regions.

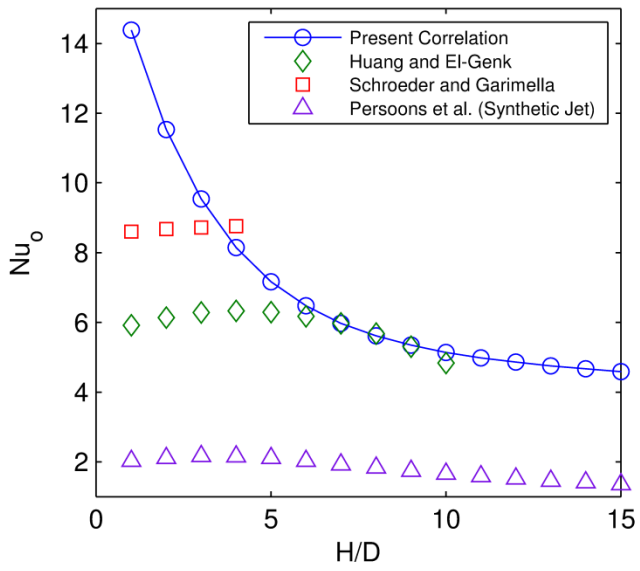

Figure 13: Comparison of stagnation correlations. The Huang and El-Genk correlation is for free jet impingement and the Schroeder and Garimella correlation is for confined jet impingement.

3.2 AREA AVERAGED HEAT TRANSFER

In order to predict thermal performance in realistic applications, the stagnation coefficient alone is insufficient. The area averaged Nusselt number (Nu_{bar}), governed by the geometry of the heat source being considered, must also be characterized. The area-averaged results are shown in Figure 14 for V_b = 8 V. The area over which the convection coefficient is averaged is circular in shape and the performance is a function of the radius (R). Note that a circular heat source with an R/D greater than 10 would call for a spacing of H/D = 35-55, while the curve representing a spacing of H/D = 25 would provide better cooling for a heat source with an R/D from 5 to 7. If an R/D of less than 5 is required, the H/D = 5 (or smaller) spacing would be the most beneficial by far. This trend is true regardless of the voltage provided to the blower.

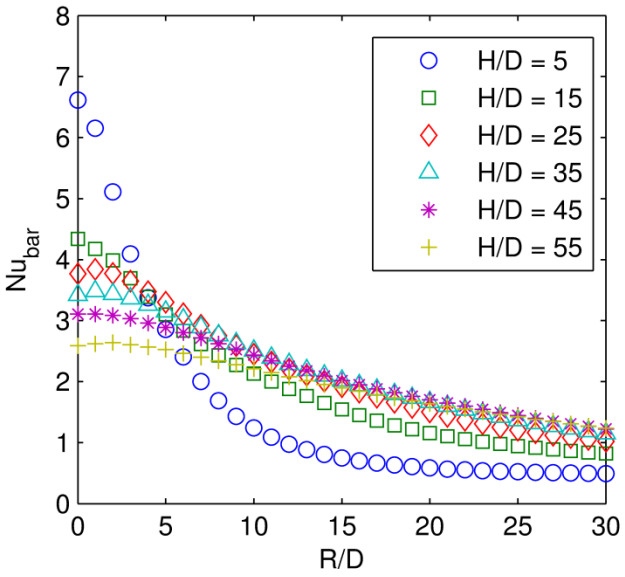

Figure 14: Area-averaged Nusselt number curve for V_b = 8 V.

We can observe the data shown in Figure 15 as a function of H/D where the V_b = 8V input is averaged over the entire 3” x 3” plate and a smaller 1” x 1” section centered about the

stagnation point. It can be seen that, for the 3” x 3” case, the average Nusselt number of the plate is lowest at about *H/D* = 3 and has a maximum at some point after *H/D* = 60. As the geometry of the heated target is modified, different curves would result, yielding a different value for optimal spacing. This can be seen in the plot of the 1” x 1” area Nu_{bar}, where the optimal distance is around *H/D* = 35 - 45. From these results, it can be seen that it is worthwhile to develop area-averaged correlations not only to predict the thermal performance, but the optimal spacing as well. This also illustrates the dependence of the optimum spacing on the heater geometry under investigation. More will be presented on this topic later.

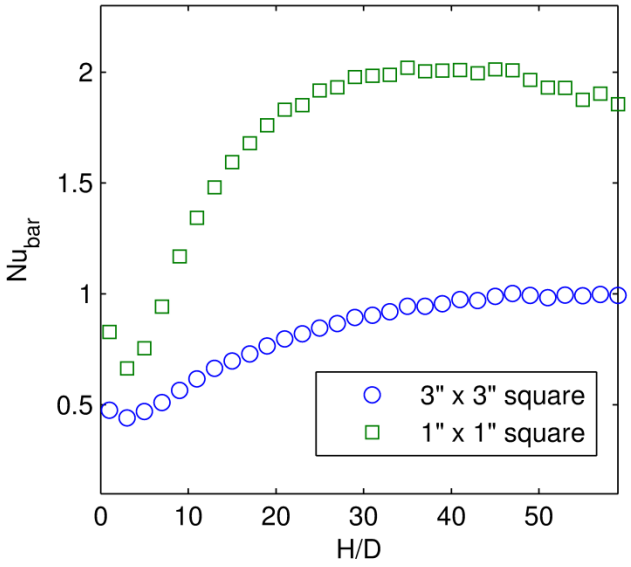

Figure 15: Average Nusselt number for the entire 76.2 mm x 76.2 mm plate as a function of spacing.

The trends seen in the area-averaged heat transfer properties are both a function of non-dimensional distance away from the heated plate and the radial area. However, this dependence can be captured with an equation of the following form (suggested by Churchill and Usagi [34]):

$$\frac{Nu_{bar}}{Nu_o} = \left[1 + \left(A_2 e^{B_2 \frac{R}{D}}\right)^{-P}\right]^{-1/P} \tag{3.7}$$

where

$$B_2 = C_2\left(\frac{H}{D}\right)^{E_2} + F_2 \tag{3.8}$$

Using a least squares curve fit, the constants were found to be A_2 = 1.08, P = 30, C_2 = -0.564, E_2 = -0.233 and F_2 = 0.201. The range where Eq. (3.8) is applicable is $1 \leq H/D \leq 59$ and $1 \leq R/D \leq 30$. It can be seen in Figure 16 (Re = 596) that the equation is verified as it is within 15% at R/D = 15 and H/D 25. It is apparent however, that larger R/D values do not compare well particularly as H/D decreases.

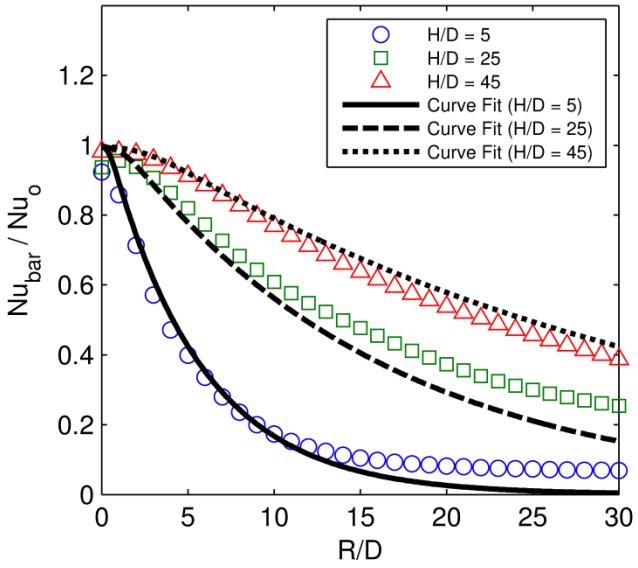

Figure 16: Area-averaged curve fit for *H/D* = 5, 25 and 45.

To determine the efficacy of the area averaged heat transfer correlations with respect to those developed by others [13-16], a plot was generated to visually compare them. Figure 17 shows that all the correlations follow the same general trend with the one presented in this thesis residing between the extreme values from the other correlations. The non-dimensional distance from the plate was set at H/D = 10 to keep it within all of their range of validity. The R/D range

was also limited to the given valid values. The only exception was with the Reynolds number; the *Re* =596 is not within the range of validity of any but the correlation developed for this thesis. However, the correlations are still within in the 50% agreement with the bulk of each other.

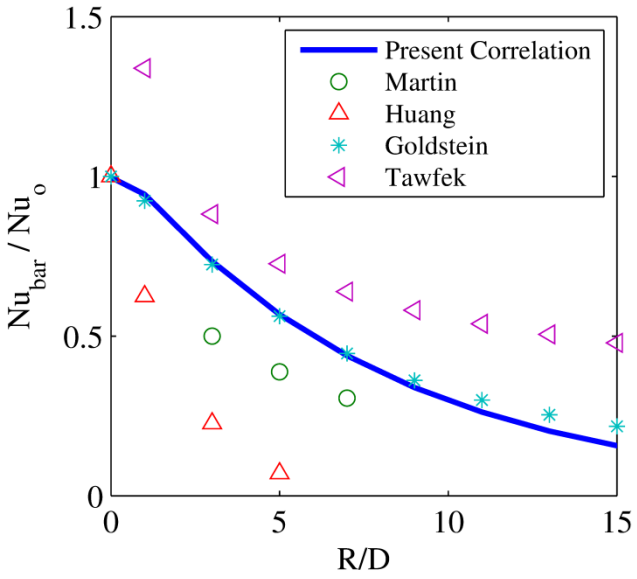

Figure 17: Comparison of the area-averaged Nusselt number correlations at *H/D* = 10 and *Re* = 596.

None of the given correlations investigated *Re* lower than 2000 [13-16], but it is interesting to note that each would predict thermal performance within a believable range for the Reynolds numbers encountered in the current work. Particularly noteworthy is the similarity between the Goldstein [14] ($61000 \leq Re \leq 124000$, $0.5 \leq R/D \leq 32$, $2 \leq H/D \leq 12$) correlation and that developed in this paper (errors less than 5%). However, this similarity no longer occurs as the distance to the heated target was increased as shown in Figure 18, where $H/D = 25$. For this case, the Tawfek correlation [16] ($3400 \leq Re \leq 41000$, $2 \leq R/D \leq 30$, $6 \leq H/D \leq 58$) best described our data. The Huang correlation [15] ($6000 \leq Re \leq 60000$, $0 \leq R/D \leq 10$, $1 \leq H/D \leq 12$) was removed for the circumstances where it diverged enough so that the solution that it gave was

no longer within reasonable bounds. The Goldstein [14] and Huang and El-Genk correlations [15] are no longer as close to the other correlations, yet the Martin [13] ($2000 \leq Re \leq 400000$, $2.5 \leq R/D \leq 7.5$, $2 \leq H/D \leq 12$) correlation is well outside of its valid H/D range, but very consistent with the Tawfek correlation [16]. It is notable that the correlation presented in this paper for the area-averaged Nusselt number (Eqs. (3.7) and (3.8)) is similar in form to traditional jet impingement correlations [13-16], namely that there is no dependence on Reynolds number once all correlations are normalized by the stagnation value.

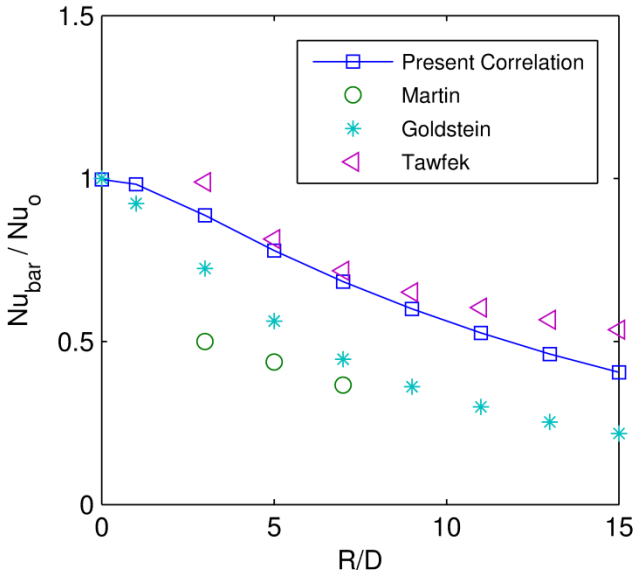

Figure 18: Comparison of the area-averaged Nusselt number correlations at *H/D* = 25 and *Re* = 596.

3.3 OPTIMUM DISTANCE

Interesting behavior is apparent when analyzing the optimum spacing as a function of the size of the heat source. This plot is provided in Figure 19 and reveals two distinct behaviors depending on the range of heat source area under consideration. The first is linear and ends around $R/D = 5$

where it abruptly transitions to a much higher optimum spacing that levels out as *R/D* becomes very large.

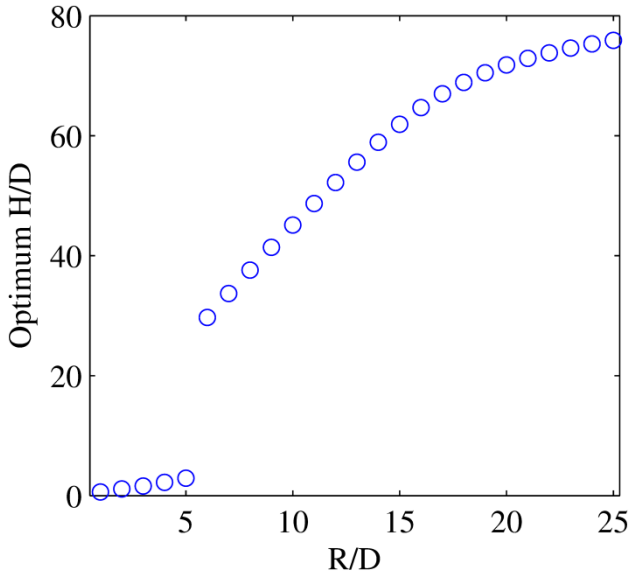

Figure 19: Optimum distance between the heat source and nozzle based on size of the cooling target. Data is generated using Eq. (3.7).

The reason for this can be observed in Figure 20 where the area-averaged Nusselt number is given for three different heater sizes (*R/D* = 4, 5, and 6). For all three, there appears to be two distinct optimum values. However, one of these (*H/D* < 6) is shown to be the dominant peak for small heat sources (*R/D* < 5), while the second peak begins to dominate the maximum performance for large heat sources (*R/D* > 5). At an approximate heat source size of *R/D* = 5, both of these peaks are nearly equal. It is important to note that Figure 19 and Figure 20 are both generated using the developed correlations (Eqs. (3.6) and (3.7)). In order to rule out an anomaly in these correlation equations, the actual experimental data was also analyzed in this way (V_b = 8V).

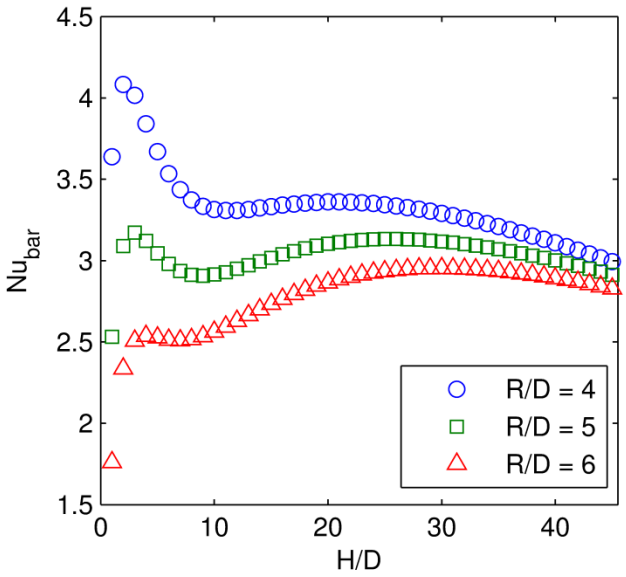

Figure 20: Area-averaged Nusselt number as a function of *H/D* for three different sizes of the cooling target (*R/D* = 4, 5 and 6).

The result is shown in Figure 21 where it is apparent that both the correlation and the comparable data exhibit the same characteristics. It is also important to note that this secondary optimum *H/D* is not observed unless lateral conduction is considered. This reinforces the notion that the effect of lateral conduction should be fully investigated before cooling optimization can occur.

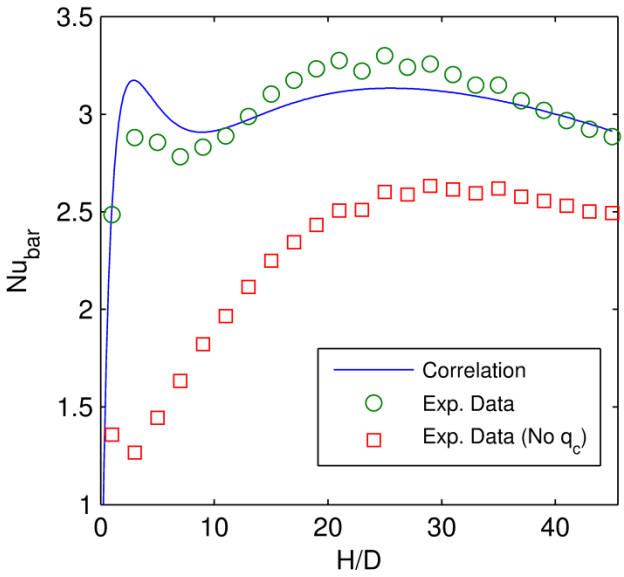

Figure 21: Comparison of the correlation with the experimental data both with and without lateral conduction.

4.0 OSCILLATING FLOW THROUGH MICROCHANNELS

The type of air mover that has been analyzed in this paper has the capability to overcome high back pressures while maintaining reasonably high flow rates. This makes it well suited to an application that utilizes microchannels. For cooling applications, however, using air in heated microchannels can lead to flow choking issues due to potentially drastic density changes within the channel. One option is to change the working fluid. Using a fluid such as water or a fluorocarbon-based fluid can mitigate the problem as well as provide a marked increase in cooling potential.

4.1 THEORY

However, the blower in this research is designed to work exclusively in air. Additionally, water will cause it to electrically short and fluorocarbon based fluids are often very expensive. A novel workaround to this problem is to use either one or a pair of blowers to create a back and forth oscillating flow (similar to an oscillating u-tube manometer). A simple illustration can be seen in Figure 22.

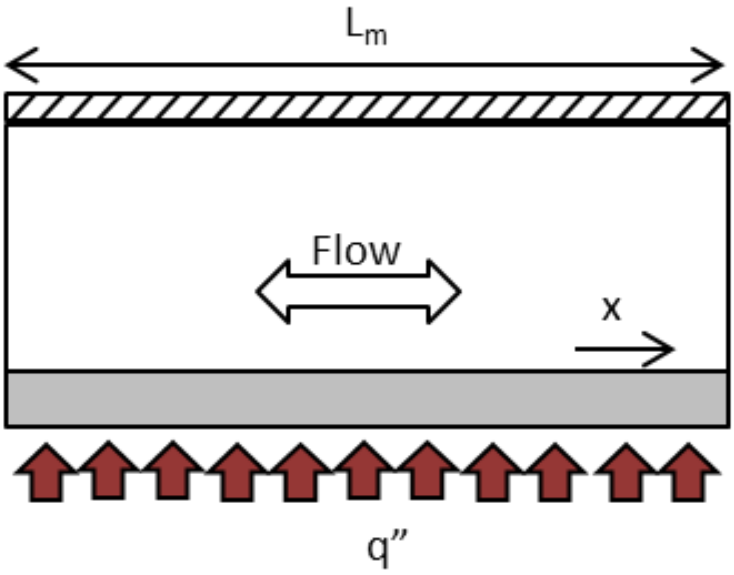

Figure 22: Generalized illustration of the potential oscillating flow system.

For the analysis to demonstrate the viability of this concept, a set of microchannels that were designed to be used in the water cooling of a computer chip will be used as a model (Figure 23).

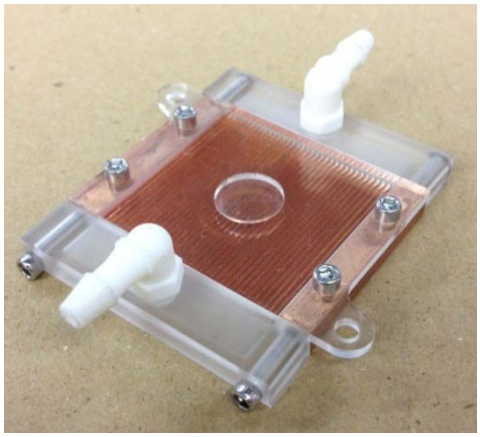

Parameter	Value
Channel Height	0.787 mm
Channel Width	0.660 mm
Channel Length	30.0 mm
Number of Channels	36

Figure 23: A photo of the set of microchannels and the corresponding dimensions.

A key assumption that must be made is that, at steady state, the fluid that exits the microchannels will be cooled sufficiently such that all heat gained while inside the microchannel is dissipated. This can potentially be accomplished via small reservoirs of liquid on either side of the microchannel openings that have some sort of additional cooling accommodations. In a sense, this type of cooling method is akin to a heat pipe. The amount of additional cooling needed would be determined by the amount of temperature rise in the fluid over each half of the oscillation cycle.

In addition to the microchannel dimensions, there are a number of other equally important parameters that have been given below in Table 2. For this analysis, water will be used as the working fluid.

Table 2: Working fluid and operating parameters used in the oscillating flow heat transfer analysis.

Parameter	**Symbol**	**Value**
Fluid Density	ρ_f	1000 kg/m^3
Specific Heat	C	4183 J/kgK
Fluid Conductivity	k_f	0.613 W/mK
Dynamic Viscosity	μ	855*10^{-6} Ns/m^2
Total Heat	Q	65 W
Volumetric Flow Rate	$\dot{V}_o$	0.12 L/min
Fluid Oscillation Frequency	ω_f	0.7 Hz

The volumetric flow rate and the oscillating frequency were determined via preliminary proof of concept experiments. In this experiment, a single piezoelectric blower was attached to a

¼ inch nylon tube. The other end of the tube was attached to the set of microchannels seen in Figure 23 with a tube of the same inner diameter connected to the other side. Both tubes were elevated in a U-shape. The blower was subjected to a square wave of the same frequency (ω) and voltage used in the impingement experiments (ω = 25.6 kHz and V_b = 9 V). The frequency of the square wave was varied to find a value that yielded the largest fluid movement. That value was found to be roughly 0.7 Hz, which corresponds to the frequency of fluid oscillation (ω_f). To determine the volumetric flow rate ($\dot{V}_o$), the highest and lowest fluid points during the oscillation were determined and used to find the total volume displaced over one half cycle. This value can then be used to find the peak volumetric flow rate if a sinusoidal flow is assumed.

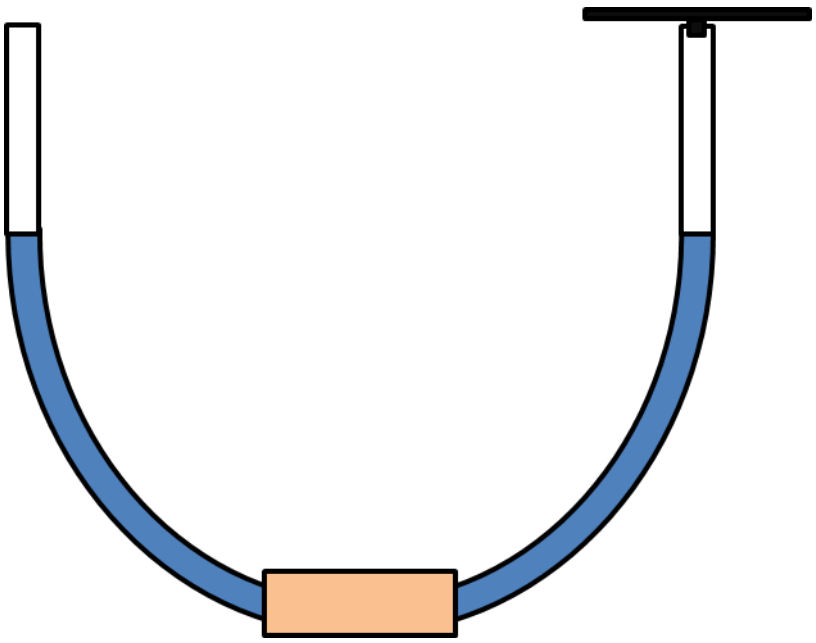

Figure 24: General representation of the proof of concept setup to determine the flow rate and oscillation frequency of the water.

Let us first consider a small slice of fluid that travels through the microchannel an incremental distance (*dx*) for an incremental unit of time (*dt*). The amount of energy imparted on the fluid will be equivalent to the caloric energy gain of the fluid:

$$q"P_{ch}dxdt = dmC\Delta T = \rho_f A_{ch} C\Delta T dx \tag{4.1}$$

where *q"* is the heat flux added to the system, P_{ch} is the perimeter of the channel, ρ_f is the fluid density, A_{ch} is the surface area of the channel, C is the specific heat, and ΔT is the temperature change of the fluid. Solving for the change in temperature and integrating with respect to time, we find:

$$\Delta T\left(t\right) = \frac{q"P_{ch}}{\rho_f A_{ch} C} t \tag{4.2}$$

This gives us an expected outcome suggesting that the rise in temperature of the fluid linearly increases in relation to the time the fluid is subjected to the heat source (assuming all parameters remain constant). At this point the only thing that needs to be determined is the amount of time that the observed piece of fluid spends in the microchannel. It is apparent that Eq. (4.2) is applicable to any piece of fluid in the channel regardless of starting location. This means that the time the slice of fluid spends in an unheated state needs to be accounted for as well. Therefore, determining the initial location of the fluid slice is the next requirement. This can be done by integrating the velocity equation spatially from the initial location (x_o) to some other x location and temporally from t = 0 to some time t. The velocity (v_o) can also be effectively approximated as a sinusoidal oscillation.

$$\int_{x_o}^{x} dx = \int_0^t v\left(t\right) dt = v_o \int_0^t sin\left(\omega_f t\right) dt \tag{4.3}$$

Integrating and solving for initial location, we find:

$$x_o = x - \frac{v_o}{\omega_f}\left(1 - cos\left(\omega_f t\right)\right) \tag{4.4}$$

Now that the initial location can be found, it can be used to determine the amount of time the packet of fluid spends not being heated before entering the microchannel. The unheated time (t_u) can be found using the same tactic that was used to find the initial location.

$$\int_{x_o}^{0} dx = \int_{0}^{t_u} v\left(t\right) dt = v_o \int_{0}^{t_u} sin\left(\omega_f t\right) dt \tag{4.5}$$

Integrating and solving for the unheated temperature (t_u):

$$t_u = \frac{1}{\omega_f} acos\left(1 + \frac{x_o \omega_f}{v_o}\right) \tag{4.6}$$

This is only applicable if the packet of fluid starts outside of the microchannel (i.e. if, for the initial first half of the cycle, x_o is negative). In the case of Eq. (4.6) used when the initial location is inside the channel, the resultant t_u will have crossed over into the imaginary region. This restriction shows that there is a limitation to the operating parameters when considering the length of the channel. This restriction can be seen as follows based off the channel length (L_m):

$$\frac{L_m \omega_f}{v_o} \leq 2 \tag{4.7}$$

If this condition is not met, it means that at least some amount of the fluid never travels outside of the channel. As this means that part of the fluid would continually be forced to receive heat, it becomes apparent how integral it would be to keep this condition met. For the current microchannel tested under the present operating conditions, Eq. (4.7) is found to be 0.822 which satisfies the condition.

4.2 LOGIC SYSTEM AND RESULTS

It is now possible to use Eqs. (4.4) and (4.6) to determine the amount of time a packet of fluid spends in the microchannel. Due to the reciprocating nature of the flow, the first three cycle halves will have to be determined separately. After the second and third oscillation cycle halves are found, they can be repeated to replicate any cycle. The first half cycle is shown in Figure 25.

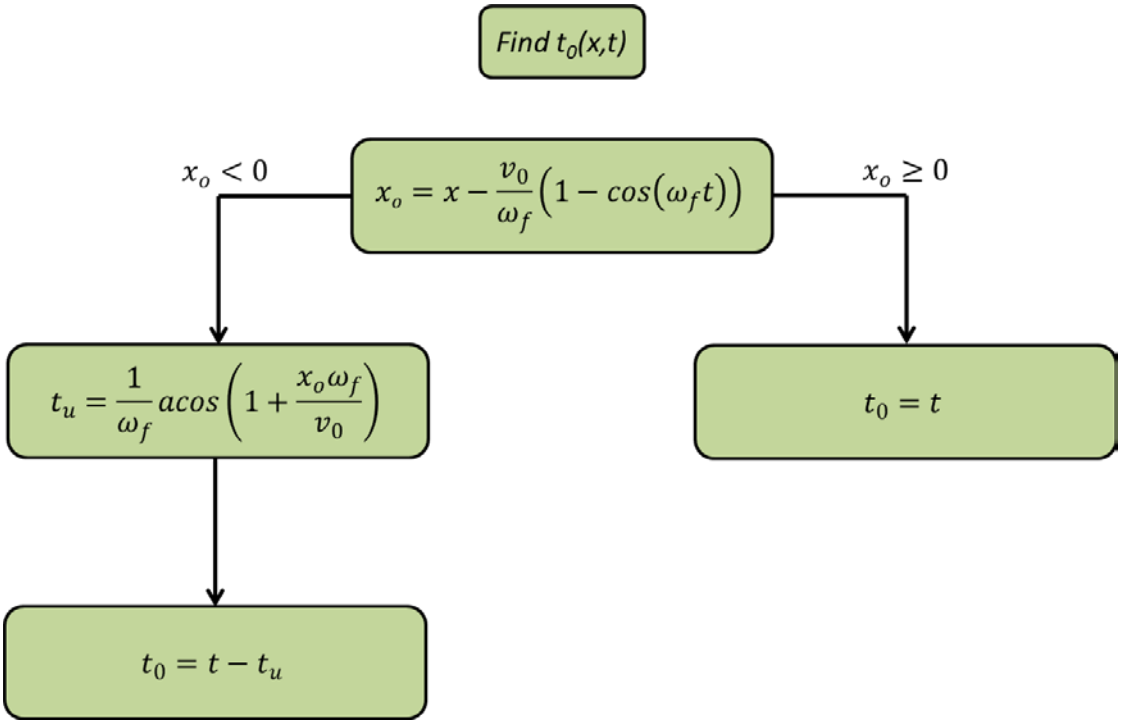

Figure 25: Logic flow chart for the determining the heated time for the first half cycle in oscillating flow.

This yields the fluid temperature progression through the channel found in Figure 26. As mentioned previously, this progression is unique to the first half cycle. The fluid temperature change starts as a constant amount at zero before being pushed out by the initial flow. Shortly after the entirety of the initial fluid is expelled from the channel, the temperature profile becomes linear (Figure 26(d)). This is what one could expect as a typical temperature profile for a

constant heat flux condition. Once the end of the first half of the cycle is approached, the temperature profile becomes curved as the fluid begins to slow down dramatically.

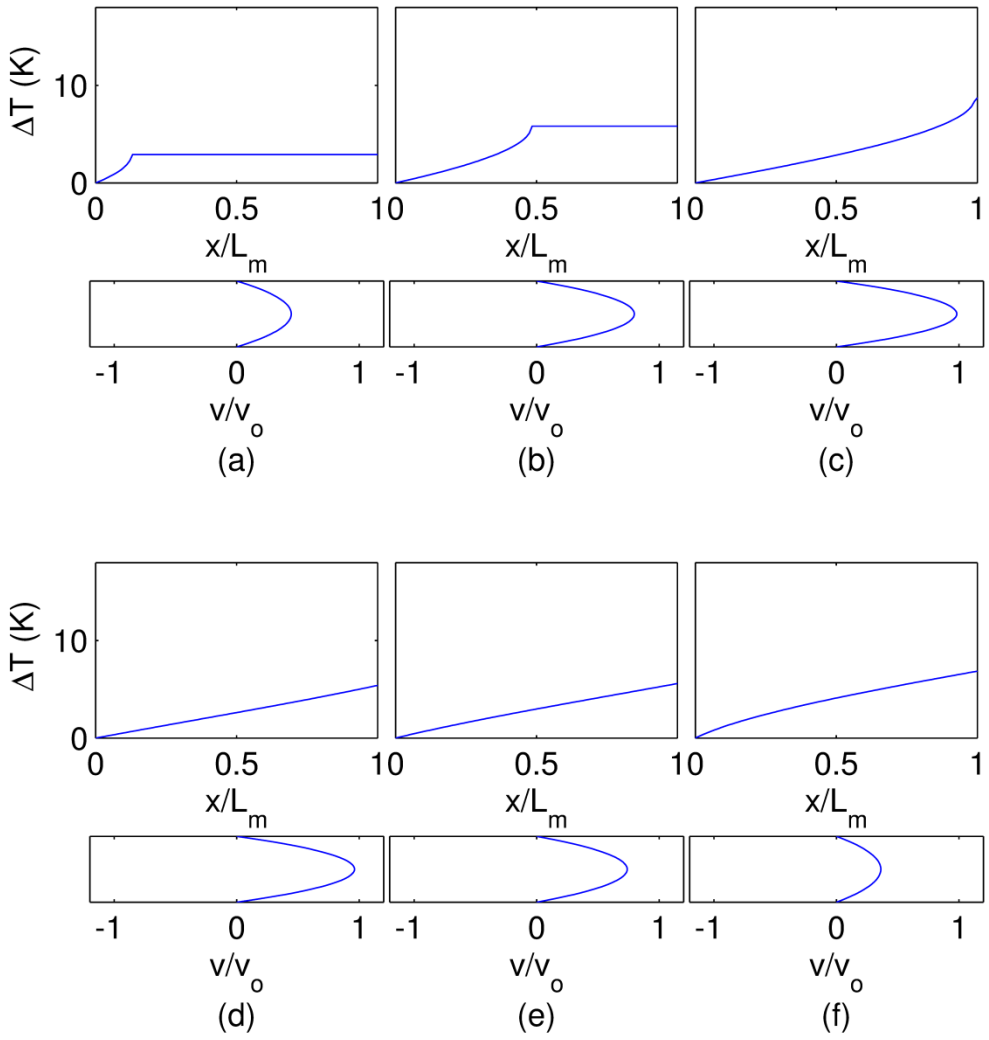

Figure 26: Fluid temperature distribution within the microchannel at $t^*\omega_f$ = (a) 0.08, (b) 0.15, (c) 0.23, (d) 0.30, (e) 0.38, and (f) 0.45.

The temperature progression for the end of the first complete cycle can be seen in Figure 27. Due to the fact that it operates with the flow moving in the reverse direction, the logic system is more complex.

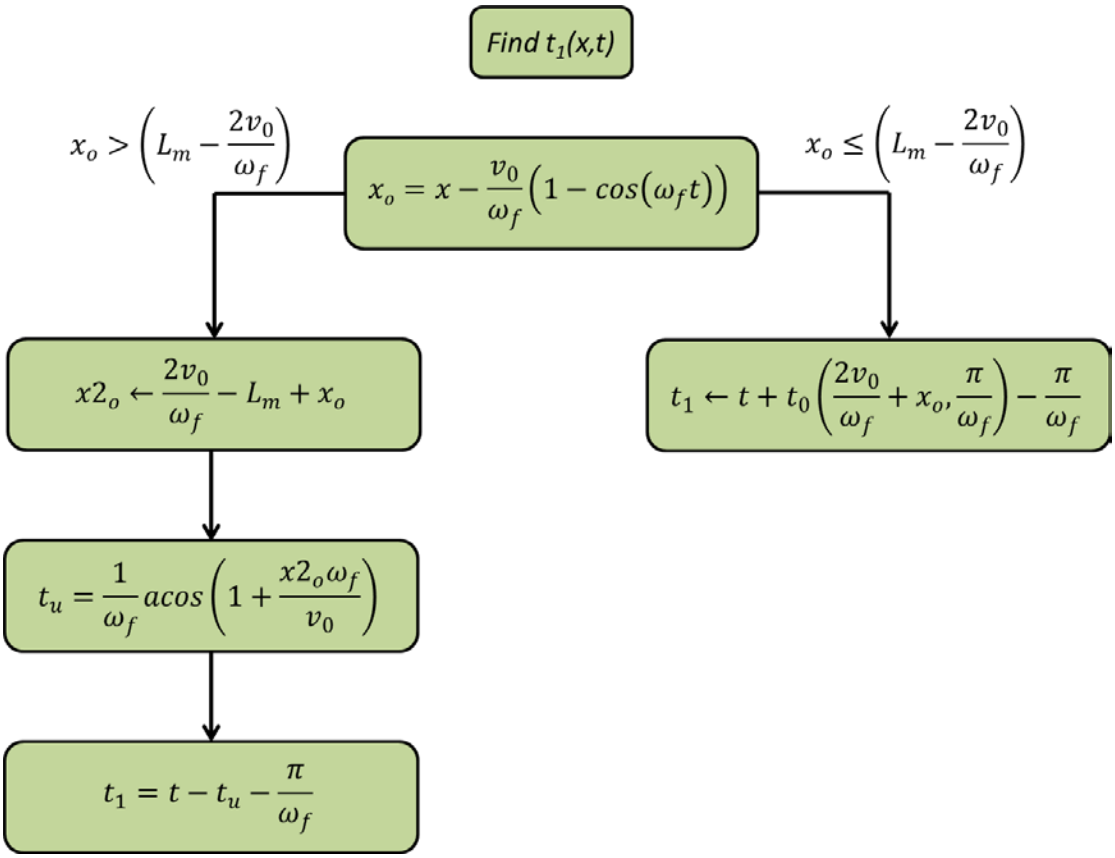

Figure 27: Logic flow chart for the determining the heated time for the second half cycle in oscillating flow.

The second half of the first cycle will yield the first indication of the maximum temperature that should be expected. Looking at Figure 28 (c), it is apparent that the maximum fluid temperature that occurs is roughly 17.5 K above inlet temperature. As in Figure 26, once the fluid that was inside the channel at the beginning of the half cycle is expelled, the temperature profile becomes simply linear with the slowing of the fluid producing a curved profile (see Figure 28(d)-(f)).

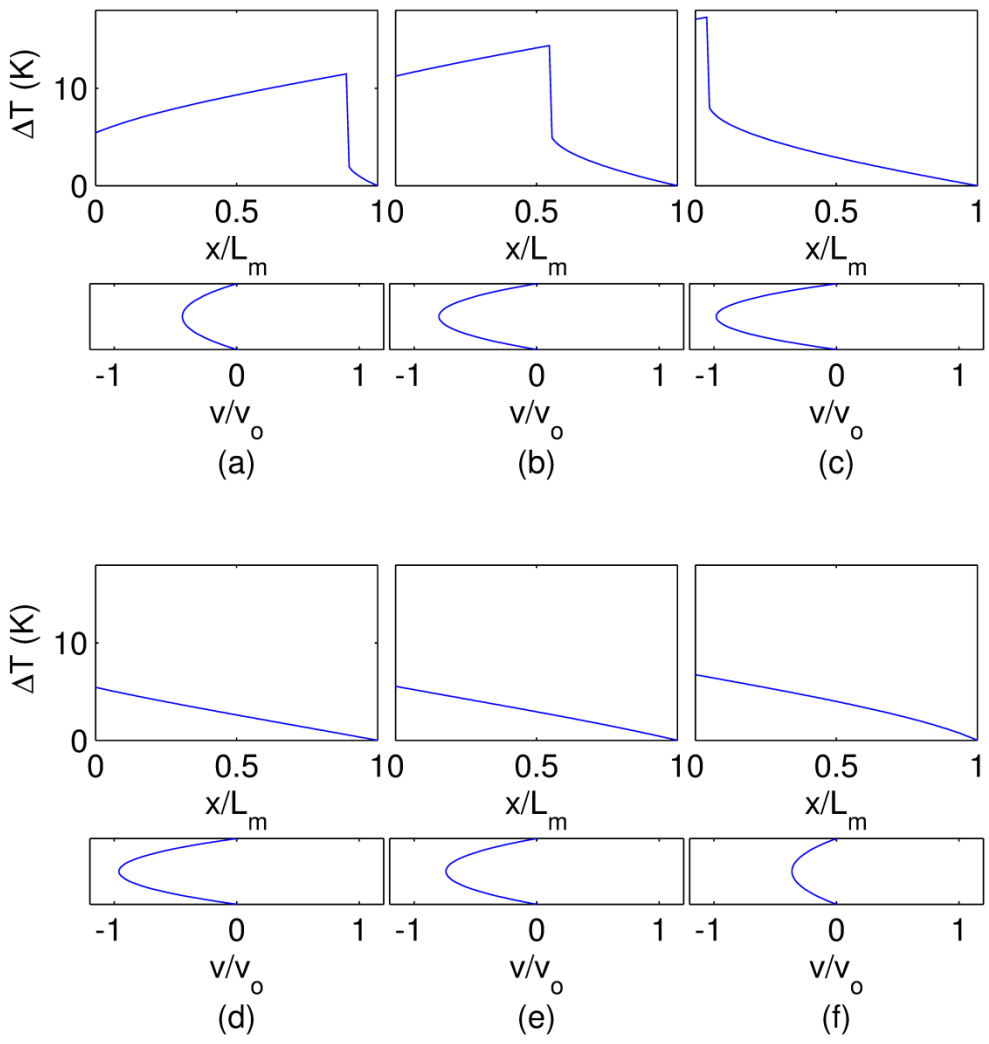

Figure 28: Fluid temperature distribution within the microchannel at $t^*\omega_f$ = (a) 0.58, (b) 0.65, (c) 0.73, (d) 0.80, (e) 0.88, and (f) 0.95.

For the third half cycle, the system used to find the heated time of the fluid (Figure 29) is very similar to that of the first half cycle. The similarities continue with the temperature profile of the fluid (seen in Figure 30) being essentially the mirror image of the temperature profile of the previous half cycle. This indicates that continuing the temperature profile through more oscillation cycles can be attained by mimicking the second and third half cycles. However, as

one would expect for this case, a new result will not be found. More specifically, after the initial half cycle, every other half cycle will be exactly the same as the previous one.

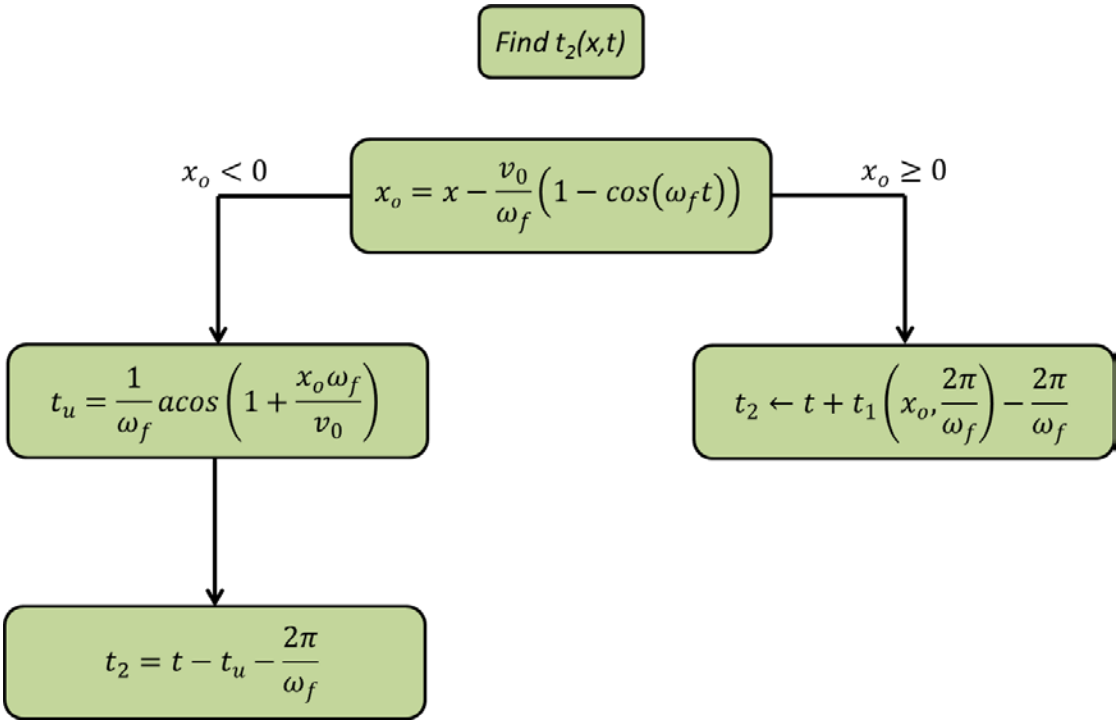

Figure 29: Logic flow chart for the determining the heated time for the third half cycle in oscillating flow.

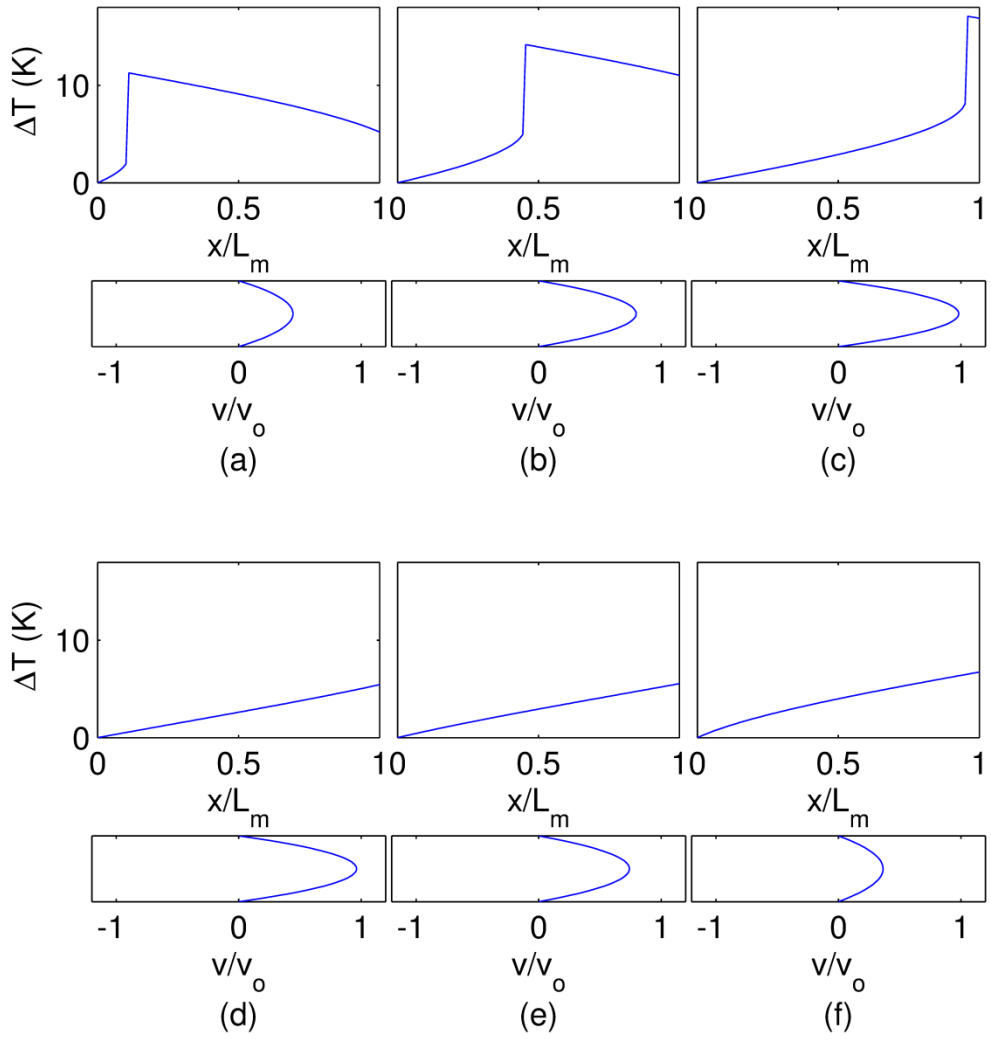

Figure 30: Fluid temperature distribution within the microchannel at $t^*\omega_f$ = (a) 1.08, (b) 1.15, (c) 1.23, (d) 1.30, (e) 1.38, and (f) 1.45.

As one would expect from flow in a heated channel, Figure 31 shows that the ends of the microchannel experience both the maximum and minimum temperature change. This occurs, expectedly, at alternating half cycles. This also means that the ends of the microchannel would experience the highest temperature variation. Note that the first half cycle displays a different temperature profile than the rest due to the difference in initial temperature shown in Figure 26.

4.3 ANALYSIS

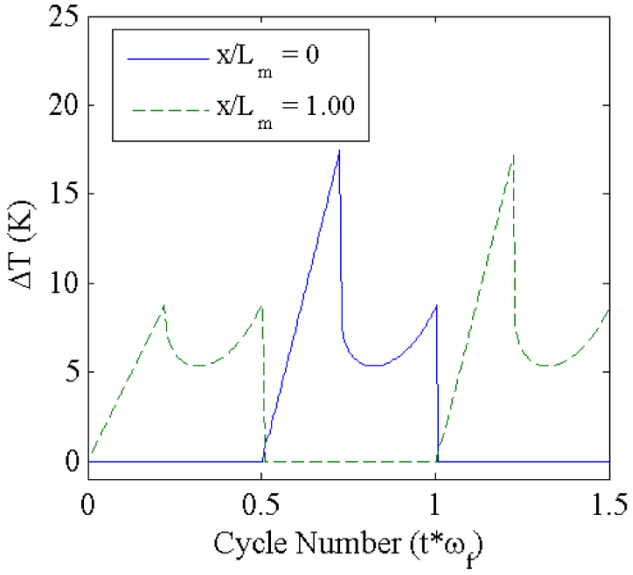

Figure 31: The temperature change progression at the ends of the channel over the first cycle and a half of oscillation.

Looking at Figure 32, the maximum temperature change seen further inside the channels is slightly less as well as no longer approaching zero. The two peaks in temperature change also start to become equal where they are exactly the same when observing the center of the channel.

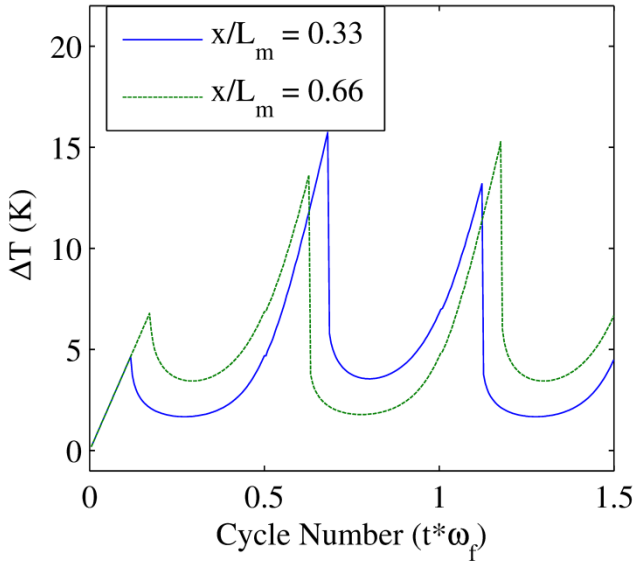

Figure 32: The temperature change progression at two intermediate points in the channel over the first cycle and a half of oscillation.

Although the maximum temperature change occurs at the ends of the channel, it can be seen from Figure 33 that the highest average temperature change occurs at the center of the channel with the ends having the lowest average temperature change. This is not unexpected due to the fact that, although the ends see the largest temperature change, the temperature change spikes only occur for a short period of time. There is also the fact that the ends experience a zero temperature change for half of a full cycle. This amounts to an average temperature change over the entire channel of roughly 4.3 K.

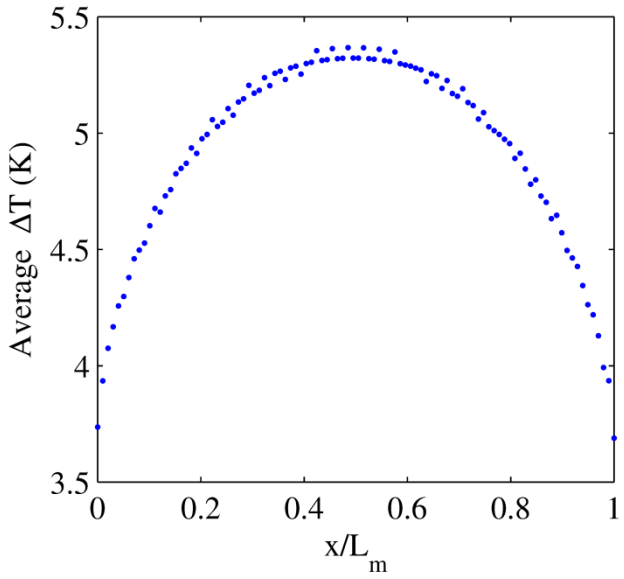

Figure 33: Cycle averaged temperature change of the fluid over the length of the channel.

Despite the relatively low average temperature change, it would be important to note that the average fluid temperature change that would occur lower in a constant flow situation. For example, observing the constant flow like situation in Figure 26(d), the average temperature change would amount to roughly 2.5 K which is 42% smaller than that found in a constant flow situation. This, understandably, shows that there are drawbacks to this type of cooling. Not only would one have to ensure that the fluid is adequately cooled once it exits the microchannel; the effective cooling performance is also less. However, this type of cooling limits the amount of fluid that is required to operate which can drastically reduce overhead costs if a fluid other than water is used (which is typical in electronics cooling applications). Further, this type of system should also yield a more consistent surface temperature due to the fluid average temperature change being more consistent. More specifically, the difference between the lowest temperature and the highest temperature of the fluid over the channel is less than that found in a constant flow

situation. This would make this type of cooling more useful in sensitive temperature situations where perhaps fatigue or performance was affected by temperature differences along the surface.

5.0 CONCLUSION AND FUTURE WORK

The heat transfer characteristics have been determined for a novel piezoelectric blower under impingement flow conditions. It was found that, for this blower, the heat transfer coefficient was dependent on distance to the target and voltage input. Correlations for the stagnation and area-averaged Nusselt number were developed and compared to traditional and synthetic jet impingement studies. This was done for a voltage input of 7, 8 and 9 volts at an *H/D* from 1 to 59. For the stagnation region, it was found that, although there was no perfect comparison between the blower and other impingement jet configurations, it was much more consistent with a continuous rather than a synthetic jet.

It was found that the maximum stagnation point Nusselt number occurs when the blower is closest to the heat source, with the performance exponentially decreasing as *H/D* increases. The near-plate performance can largely be explained by considering the lateral conduction in the data analysis. In other words, large amounts of heat are conducting towards the stagnation point due to the large temperature gradient. This finding asserts that, although one can limit the lateral conduction, the influence is still apparent and can be a significant influence under certain circumstances, especially for low flow situations. The voltage input was found to have limited effect on the Reynolds number, and therefore heat transfer capabilities, at the range considered in this work.

An optimum distance between the nozzle and heat source was determined based on size of the heater. A heat source size of roughly 5 nozzle diameters in size was seen to be a transition point between small and large optimal *H/D* values. This means that the general notion of increasing the *H/D* in direct relation to the size of the heated surface is not entirely applicable with the blower analyzed in this thesis.

The blower was also analyzed as a driver of heat transfer via oscillating flow in a microchannel. It was found that the ends of the microchannel experience the highest fluid temperature change and the lowest cycle average temperature change. The temperature change averaged over the entire channel is higher than that found in a continuous flow of the same magnitude, but the variation in average fluid temperature along the length of the channel was more uniform. This indicates that, although it does not result in as much cooling potential, oscillating flow cooling may be more beneficial for applications where the surface temperature was more sensitive to variations.

There is still quite a bit that can be analyzed with regards to this piezoelectric blower. Impingement flow is a very important aspect of cooling and was shown to be effective with this blower, however there are many more orientations and situations that could be addressed. For example, as this blower was created in large part to be used in low profile situations where space is limited, it would be prudent to look at the cooling effectiveness in that condition. It would also be important to take the theoretical analysis of oscillatory flow heat transfer and verify it with experimental work. There are also other situations that could make good use of the blower's high flow rate and pressure capabilities. Essentially, the range of possibilities has yet to be fully realized and their remains a wealth of information that one could gather from these novel piezoelectric blowers.

APPENDIX A

COMPARISON OF BLOWER VOLTAGE INPUTS

The compilation of this thesis entailed multiple snapshots of the temperature over a heated plate. The following figures are the temperature maps and resulting convection heat transfer maps once every mode of heat transfer is taken into account. The two blower voltage inputs are V_b = 7 V and 9 V in order to facilitate a visual comparison of the difference when more flow is delivered.

A.1 TEMPERATURE MAPS

As one would expect, the temperature map is a vital component of determining the convection heat transfer coefficient and thus resulting cooling performance. The following is a comparison at different *H/D* levels in order to visualize the difference between the effect each blower voltage input has.

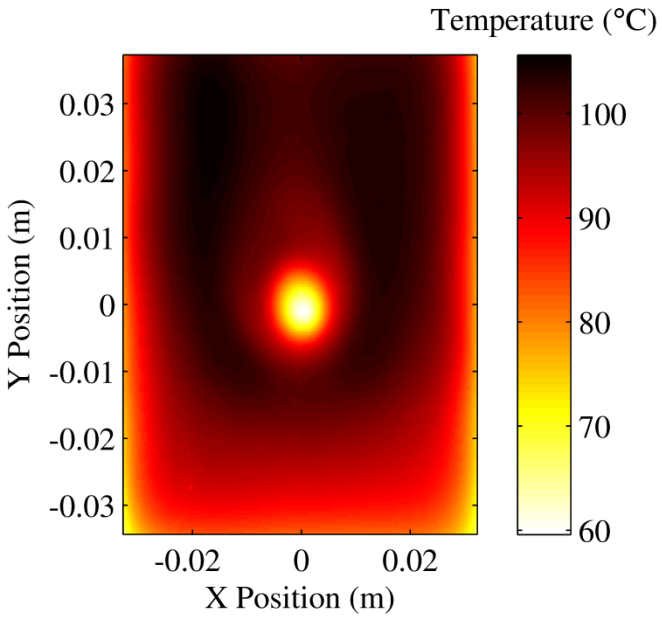

(a)

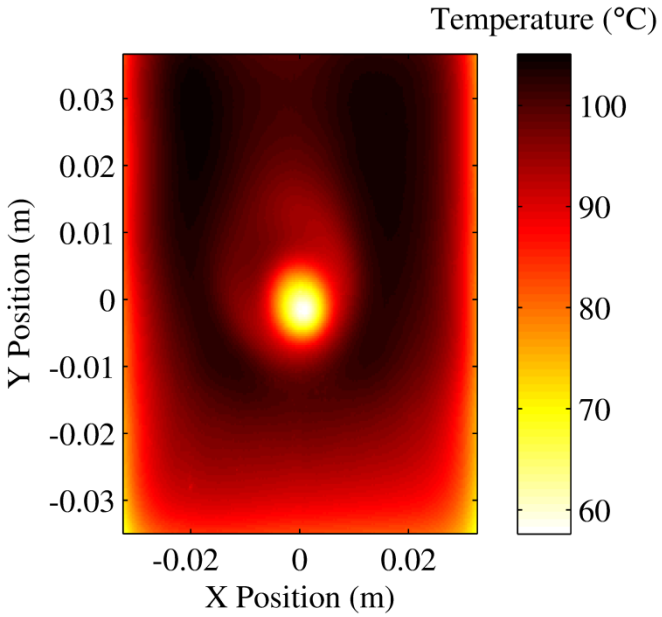

(b)

Figure 34: Temperature map of the V_b = (a) 7 V and (b) 9 V for *H/D* = 3.

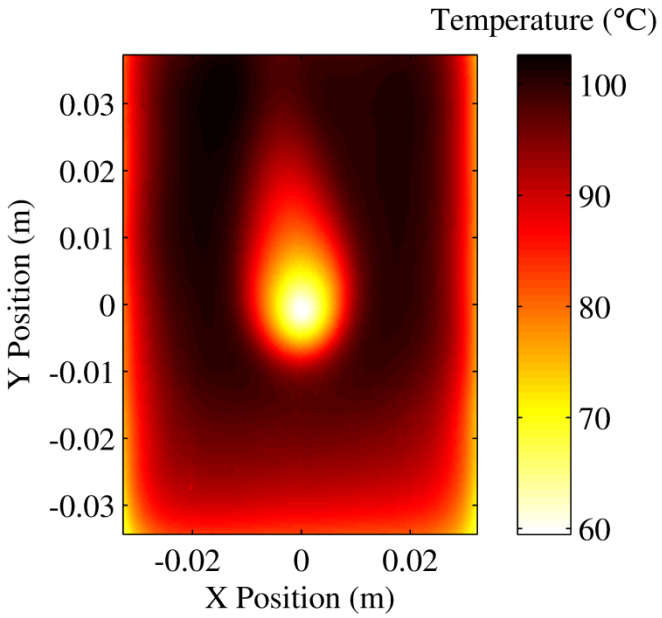

(a)

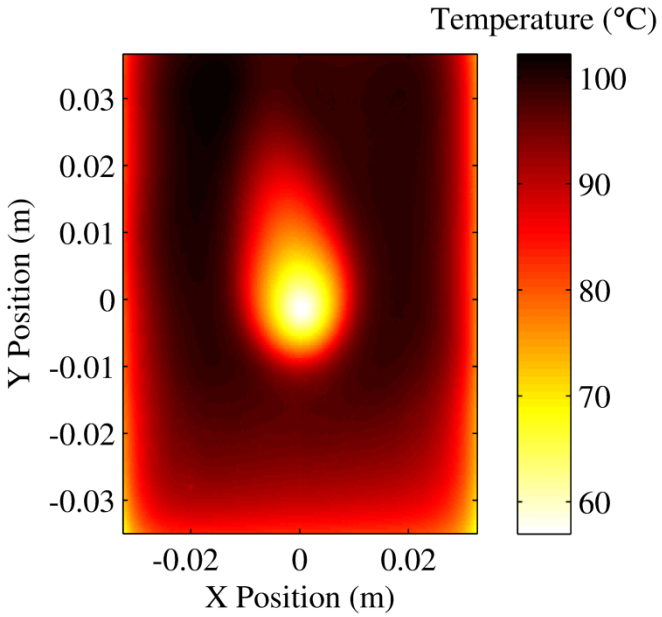

(b)

Figure 35: Temperature map of the V_b = (a) 7 V and (b) 9 V for *H/D* = 7.

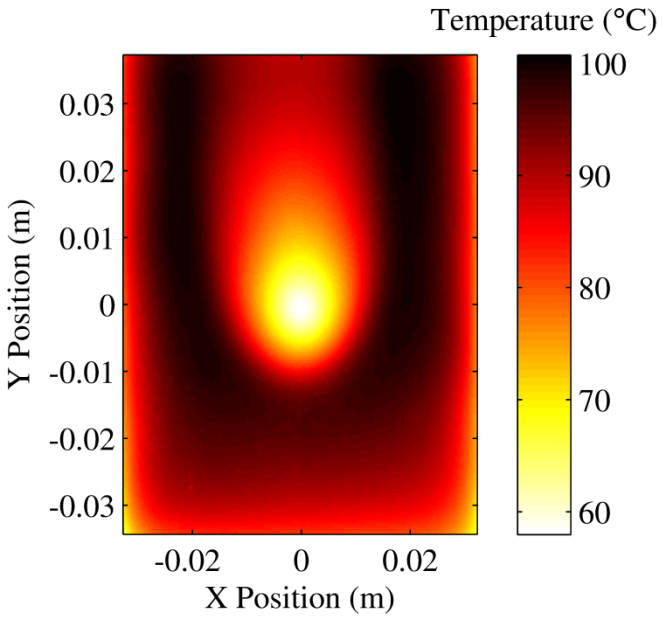

(a)

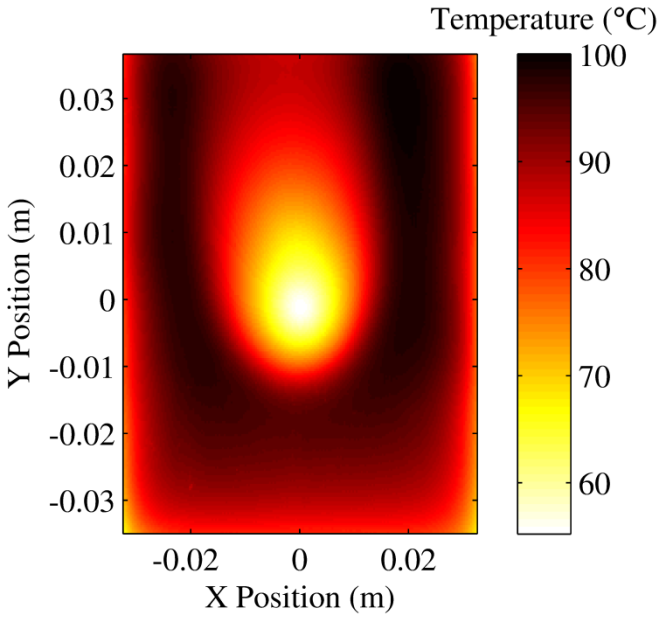

(b)

Figure 36: Temperature map of the V_b = (a) 7 V and (b) 9 V for *H/D* = 11.

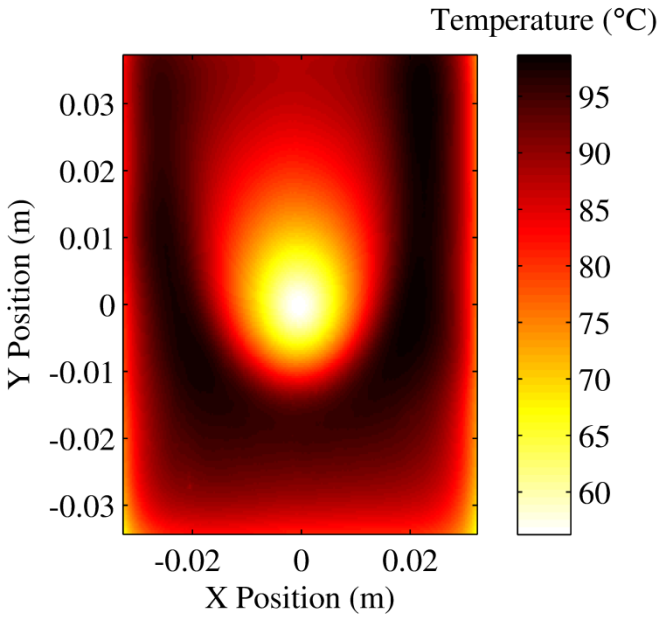

(a)

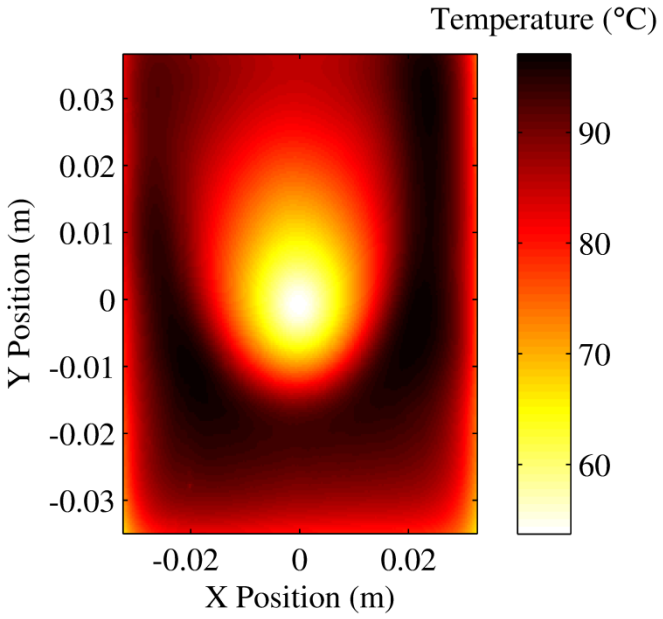

(b)

Figure 37: Temperature map of the V_b = (a) 7 V and (b) 9 V for *H/D* = 15.

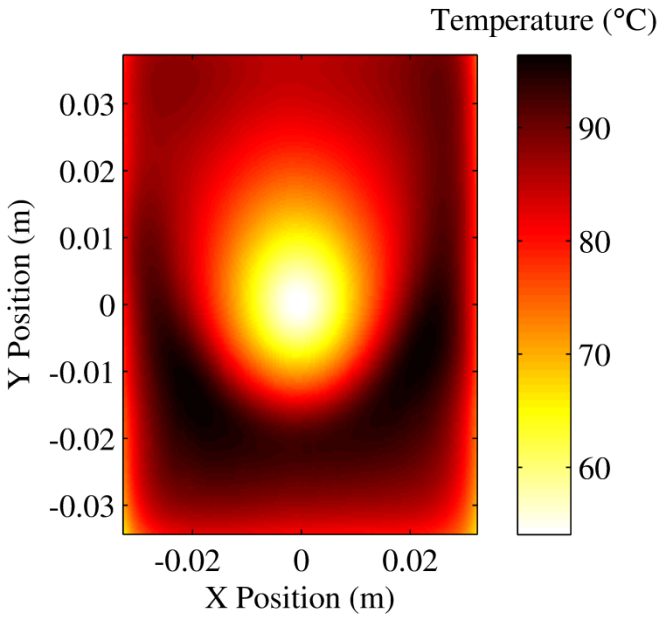

(a)

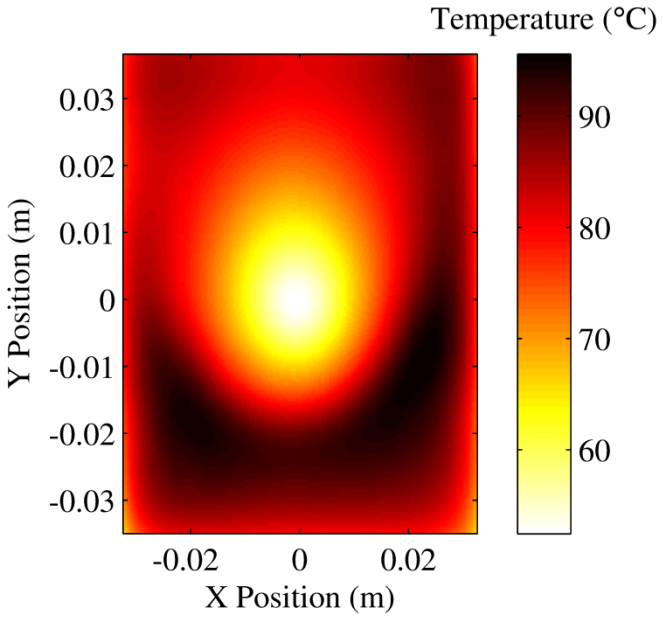

(b)

Figure 38: Temperature map of the V_b = (a) 7 V and (b) 9 V for *H/D* = 25.

A.2 HEAT TRANSFER COEFFICIENT MAP

As discussed in the thesis, the temperature map is used to determine a map of the convection heat transfer coefficient. It can be observed that the color profile is much narrower than the temperature map. This can be attributed in part to the lateral conduction in the thin film. Also note that the colorbar limit was increased on the 9V case due to the much larger heat transfer coefficient in the low *H/D* range.

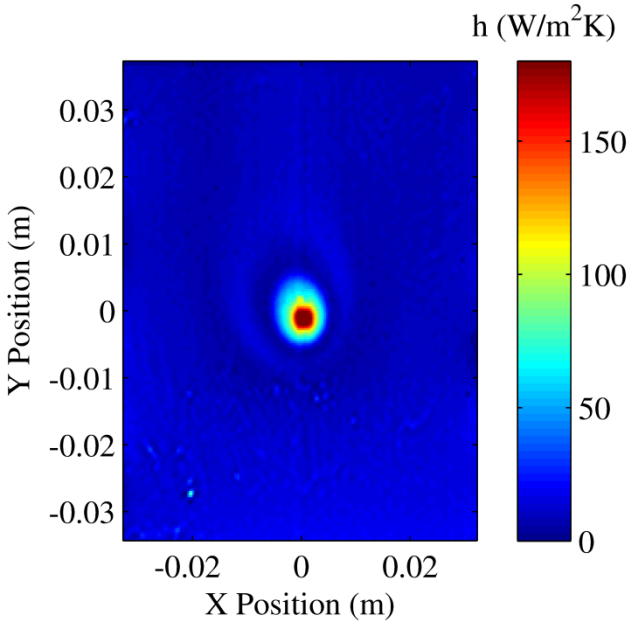

(a)

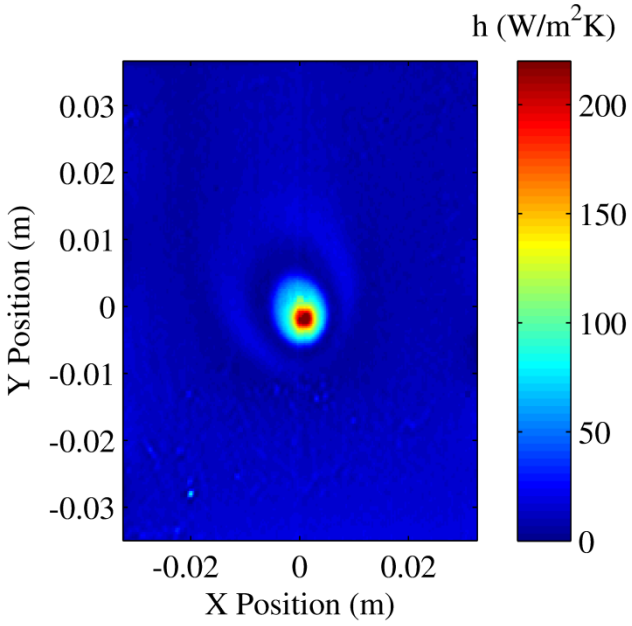

(b)

Figure 39: Convection heat transfer map of the V_b = (a) 7 V and (b) 9 V for *H/D* = 3.

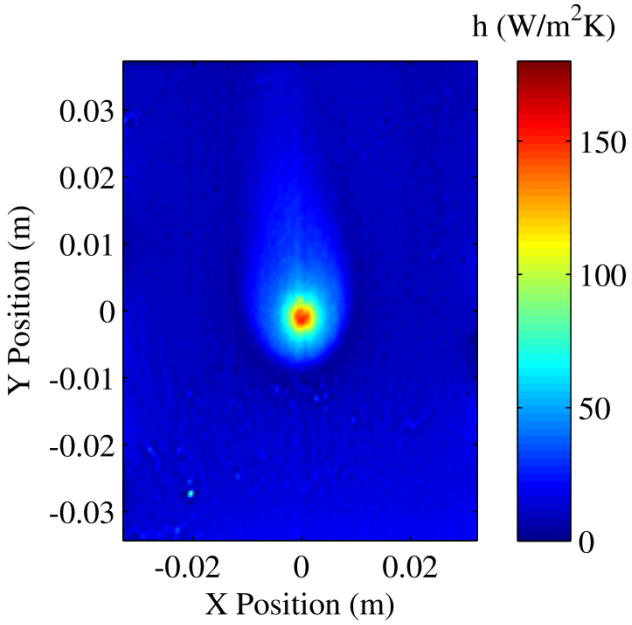

(a)

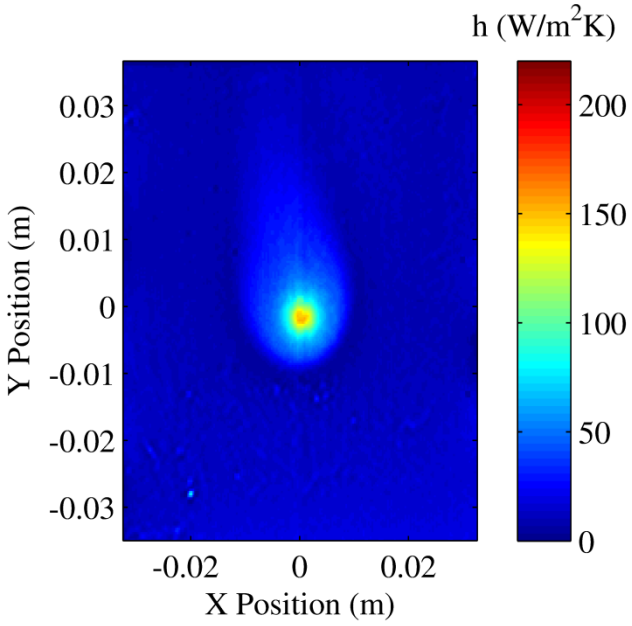

(b)

Figure 40: Convection heat transfer map of the V_b = (a) 7 V and (b) 9 V for *H/D* = 7.

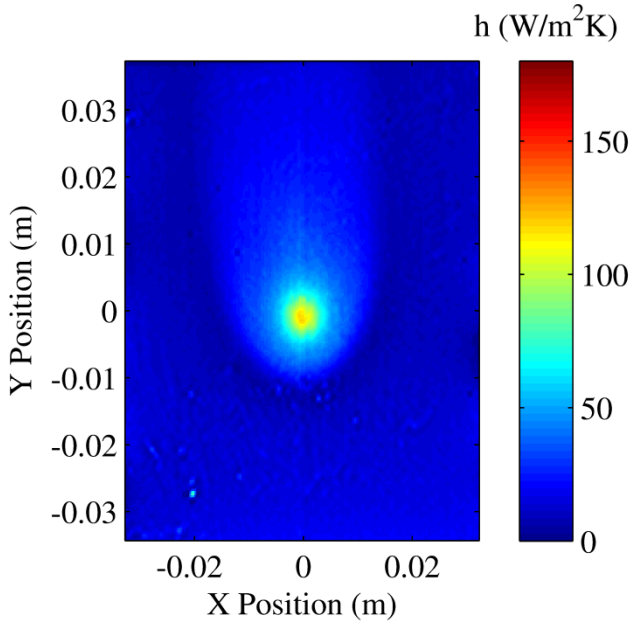

(a)

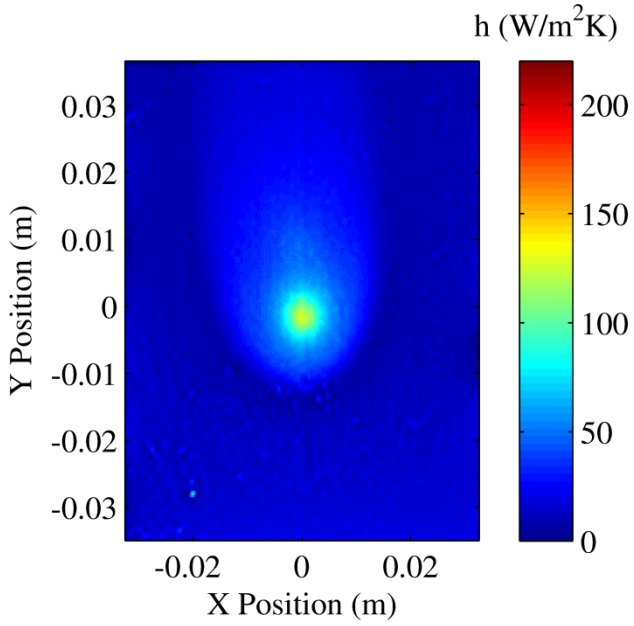

(b)

Figure 41: Convection heat transfer map of the V_b = (a) 7 V and (b) 9 V for *H/D* = 11.

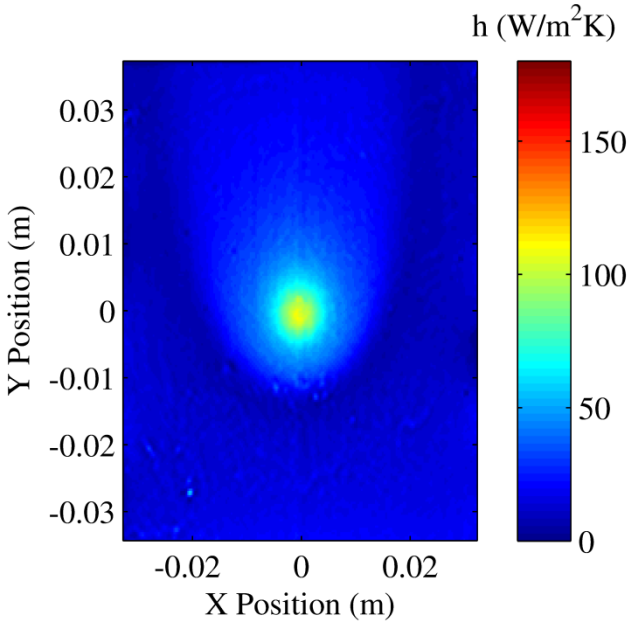

(a)

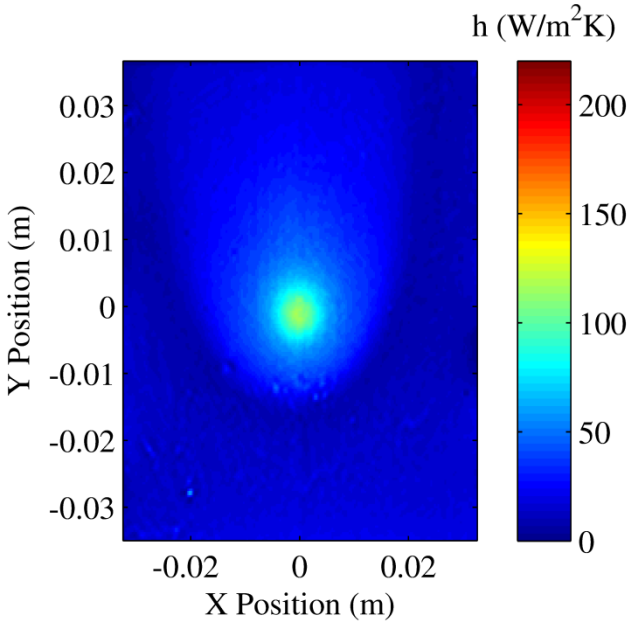

(b)

Figure 42: Convection heat transfer map of the V_b = (a) 7 V and (b) 9 V for *H/D* = 15.

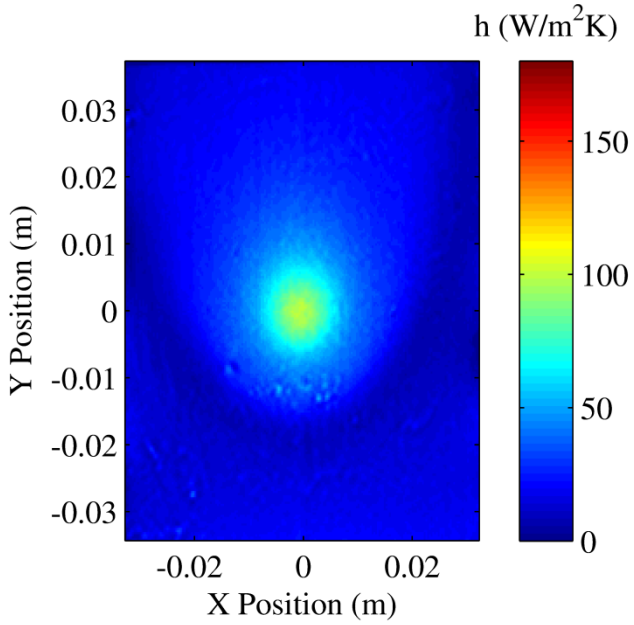

(a)

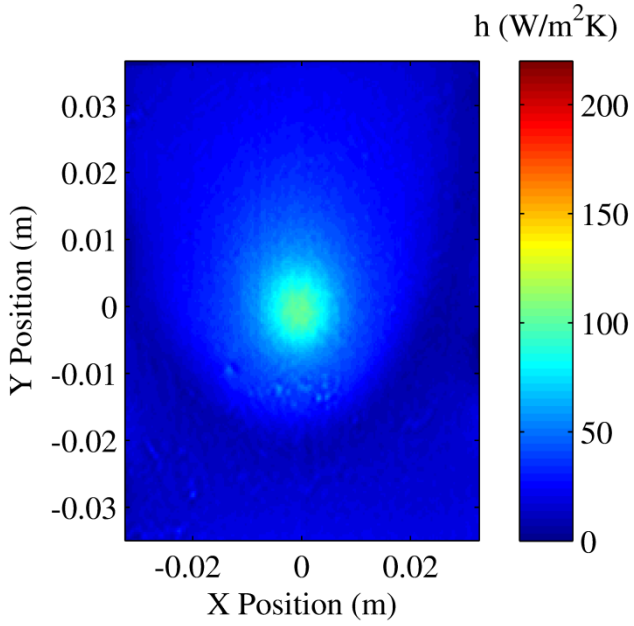

(b)

Figure 43: Convection heat transfer map of the V_b = (a) 7 V and (b) 9 V for *H/D* = 25.

APPENDIX B

BREAKDOWN OF THE UNCERTAINTY ANALYSIS

For all uncertainty, the repeatability uncertainty was determined using a simple t-test of which the form is:

$$u_r = \frac{t_{0.95} S}{\sqrt{N}} \tag{7.1}$$

where (u) is the uncertainty, ($t_{0.95}$) is the "t" value based on the sample size at 95% confidence, (S) is the standard deviation and (N) is the number of samples. Where applicable, the precision and repeatability uncertainty were combined using the following equation:

$$u = \sqrt{u_r^{\,2} + u_p^{\,2}} \tag{7.2}$$

This yields the following uncertainties for each factor taken into account and can be seen in Table 3 (Note: this is a representative sample based on a single H/D = 11 at the stagnation point):

Table 3: List of the uncertainty breakdown of various variables that were captured for this analysis.

Factor	Precision Uncertainty	Repeatability Uncertainty	*N*	Total Uncertainty	Units	Percentage
A	0.00085	-	-	0.00085	m^2	1.5%
I_s	0.15	0.062	200	0.216	Amp	0.7%
V_s	0.0015	0.00008	200	0.00158	Volt	0.3%
T_s	1	0.17	9	1.17	K	3.7%
T_∞	$9.5x10^{-9}$	0.0043	120	0.0043	K	0.001%
k_a	0.0005	-	-	0.0005	W/mK	1.9%
h_{nc}	0.55	-	-	0.55	W/m^2K	8.0%
D	0.00005	-	-	0.00005	m	5.0%

Once those values were determined, the combined uncertainty for temperature change, local heat generation, and radiation heat loss were found using the following equations:

$$u_{\Delta T} = \sqrt{\left(u_{T_s}\frac{\partial \Delta T}{\partial T_s}\right)^2 + \left(u_{T_\infty}\frac{\partial \Delta T}{\partial T_\infty}\right)^2} \tag{7.3}$$

$$u_{Q_t} = \sqrt{\left(u_C\frac{\partial Q_t}{\partial C}\right)^2 + \left(u_V\frac{\partial Q_t}{\partial V}\right)^2 + \left(u_A\frac{\partial Q_t}{\partial A}\right)^2} \tag{7.4}$$

$$u_{Q_r} = \sqrt{\left(u_{T_s}\frac{\partial Q_r}{\partial T_s}\right)^2 + \left(u_{T_\infty}\frac{\partial Q_r}{\partial T_\infty}\right)^2} \tag{7.5}$$

which, ends up being 1.17 K, 42 W/m^2, and 19 W/m^2 respectively.

The lateral conduction uncertainty was determined based on the surface temperature uncertainties and can be determined by:

$$u_{Q_c} = \sqrt{\left(u_{T_{m,n+1}}\frac{\partial Q_c}{\partial T_{m,n+1}}\right)^2 + \left(u_{T_{m,n-1}}\frac{\partial Q_c}{\partial T_{T_{m,n-1}}}\right)^2 + \left(u_{T_{m+1,n}}\frac{\partial Q_c}{\partial T_{m+1,n}}\right)^2 + \left(u_{T_{m-1,n}}\frac{\partial Q_c}{\partial T_{T_{m-1,n}}}\right)^2 + \left(u_{T_{m,n}}\frac{\partial Q_c}{\partial T_{T_{m,n}}}\right)^2} \tag{7.6}$$

which can be found to be 47 W/m^2 at the stagnation point. This same basic idea continues as the heat transfer coefficient uncertainty is determined by:

$$u_h = \sqrt{\left(u_{Q_t}\frac{\partial h}{\partial Q_t}\right)^2 + \left(u_{Q_r}\frac{\partial h}{\partial Q_r}\right)^2 + \left(u_{Q_c}\frac{\partial h}{\partial Q_c}\right)^2 + \left(u_{h_{nc}}\frac{\partial h}{\partial h_{nc}}\right)^2 + \left(u_{\Delta T}\frac{\partial h}{\partial \Delta T}\right)^2} \tag{7.7}$$

which yields an uncertainty of 4.0 W/m^{2}K.

Again, this is continued with the Nusselt number which gives the following equation:

$$u_{Nu} = \sqrt{\left(u_h\frac{\partial Nu}{\partial h}\right)^2 + \left(u_D\frac{\partial Nu}{\partial D}\right)^2 + \left(u_{k_a}\frac{\partial Nu}{\partial k_a}\right)^2} \tag{7.8}$$

which ultimately yields a stagnation Nusselt number uncertainty of 0.3 or 6.6%.

BIBLIOGRAPHY

1. Ribeiro, M.F.T., J.L.M. Santos, and J.L.F.C. Lima, *Piezoelectric Pumping in Flow Analysis: Application to the Spectrophotometric Determination of Gabapentin.* Analytica Chimica Acta, 2007. **600**: p. 14-20.

2. Cheng, G.-M., et al., *Piezoelectric Pump Used in Bionic Underwater Propulsion Unit.* Journal of Bionic Engineering, 2007. **4**: p. 159-164.

3. Gerlach, T., M. Schuenemann, and H. Wurmus, *A New Micropump Principle of the Reciprocating Type Using Pyramidic Micro Flowchannels as Passive Valves.* Journal of Micromechanical Microengineering, 1995. **5**: p. 199-201.

4. Gerlach, T. and H. Wurmus, *Working Principle and Performance of the Dynamic Micropump.* Sensors and Actuators, 1995. **50**: p. 135-140.

5. Olsson, A., G. Stemme, and E. Stemme, *A Numerical Design Study of the Valveless Diffuser Pump Using a Lumped Mass Model.* Journal of Micromechanical Microengineering, 1999. **9**: p. 34-44.

6. Ullmann, A., *The Piezoelectric Valve-Less Pump--Performance Enhancement Analysis.* Sensors and Actuators, 1998. **69**: p. 97-105.

7. Olsson, A., G. Stemme, and E. Stemme, *A Valve-Less Planar Fluid Pump with Two Pump Chambers.* Sensors and Actuators, 1995. **46-47**: p. 549-556.

8. Smith, B.L. and A. Glezer, *The Formation and Evolution of Synthetic Jets.* Physics of Fluids, 1998. **10**(9): p. 2281-2297.

9. Pavlova, A. and M. Amitay, *Electronic Cooling Using Synthetic Jet Impingement.* Journal of Heat Transfer, 2006. **128**(9): p. 897-907.

10. Chaudhari, M., B. Puranik, and A. Agrawal, *Heat Transfer Characteristics of Synthetic Jet Impingement Cooling.* International Journal of Heat and Mass Transfer, 2010. **53**: p. 1057-1068.

11. Utturkar, Y., et al., *A Jet Formation Criterion for Synthetic Jet Actuators,* , in *41st Aerospace Sciences Meeting and Exhibit* 2003: Reno, NV. p. 1-9.

12. Valiorgue, P., et al., *Heat Transfer Mechanisma in an Impinging Synthetic Jet for a Small Jet-to-Surface Spacing.* Experimental Thermal and Fluid Science, 2009. **33**(4): p. 597-603.

13. Martin, H., *Heat and Mass Transfer Between Impinging Gas Jets and Solid Surfaces*, in *Advances in Heat Transfer*, T. Irvin and J.P. Hartnett, Editors. 1977, Academic Press: New York. p. 1-60.

14. Goldstein, R.J., A.I. Behbahani, and K.K. Heppelmann, *Streamwise Distribution of the Recovery Factor and the Local Heat Transfer Coefficient to an Impinging Circular Air Jet.* International Journal of Heat and Mass Transfer, 1986. **29**(8): p. 1227-1235.

15. Huang, L. and M.S. El-Genk, *Heat Transfer of an Impinging Jet on a Flat Surface.* International Journal of Heat and Mass Transfer, 1994. **37**(13): p. 1915-1923.

16. Tawfek, A.A., *Heat Transfer and Pressure Distributions of an Impinging Jet on a Flat Surface.* Heat and Mass Transfer, 1996. **32**: p. 49-54.

17. Chiriac, V.A. and A. Ortega, *A Numerical Study of the Unsteady Flow and Heat Transfer in a Transitional Confined Slot Jet Impinging on an Isothermal Surface.* International Journal of Heat and Mass Transfer, 2002. **45**(6): p. 1237-1248.

18. Persoons, T., A. McGuinn, and D.B. Murray, *A General Correlation for the Stagnation Point Nusselt Number of an Axisymmetric Impinging Synthetic Jet.* International Journal of Heat and Mass Transfer, 2011. **54**: p. 9.

19. Lytle, D. and B.W. Webb, *Air Jet Impingement Heat Transfer at Low Nozzle-Plate Spacings.* International Journal of Heat and Mass Transfer, 1994. **37**(12): p. 1687-1697.

20. Kendoush, A.A., *Theory of Stagnation Region Heat Transfer to Fluid Jets Impinging Normally on Solid Surfaces.* Chemical Engineering and Processing, 1998. **37**: p. 223-228.

21. San, J.-Y. and W.-Z. Shiao, *Effects of Jet Plate Size and Plate Spacing on the Stagnation Nusselt Number for a Confined Circular Air Jet Impinging on a Flat Surface.* International Journal of Heat and Mass Transfer, 2006. **49**: p. 3477-3486.

22. Li, C.-Y. and S.V. Garimella, *Prandtl-Number Effects and Generalized Correlations for Confined and Submerged Jet Impingement.* International Journal of Heat and Mass Transfer, 2001. **44**: p. 3471-3480.

23. Schroeder, V.P. and S.V. Garimella. *Heat Transfer from a Discrete Heat Source in Confined Air Jet Impingement.* in *11th International Heat Transfer Conference*. 1998. Kyongju, Korea: Heat Transfer.

24. Garimella, S.V. and R.A. Rice, *Confined and Submerged Liquid Jet Impingement Heat Transfer.* Journal of Heat Transfer, 1995. **117**(4): p. 871-877.

25. Lin, Z.H., Y.J. Chou, and Y.H. Hung, *Heat Transfer Behaviors of a Confined Slot Jet Impingement.* International Journal of Heat and Mass Transfer, 1997. **40**(5): p. 1095-1107.

26. San, J.-Y., C.-H. Huang, and M.-H. Shu, *Impingement Cooling of a Confined Circular Air Jet.* International Journal of Heat and Mass Transfer, 1997. **40**(6): p. 1355-1364.

27. Fitzgerald, J.A. and S.V. Garimella, *A Study of the Flow Field of a Confined and Submerged Impinging Jet.* International Journal of Heat and Mass Transfer, 1998. **41**: p. 1025-1034.

28. Kurzweg, U.H., *Enhanced Heat Conduction in Oscillating Viscous Flows Within Parallel-Plate Channels.* Journal of Fluid Mechanics, 1985. **156**: p. 291-300.

29. Zhao, T. and P. Cheng, *A Numerical Solution of Laminar Forced Convection in a Heated Pipe Subjected to a Reciprocating Flow.* International Journal of Heat and Mass Transfer, 1995. **38**(16): p. 3011-3022.

30. Akdag, U. and A.F. Ozguc, *Experimental Investigation of Heat Transfer in Oscillating Annular Flow.* International Journal of Heat and Mass Transfer, 2009. **52**: p. 2667-2672.

31. *NASA Jet Propulsion Laboratory Website*. 2003 4/4/2003 [cited 2010 8/19/2010]; Available from: http://masterweb.jpl.nasa.gov/reference/paints.htm.

32. Jordan, T., et al., *Electrical Properties and Power Considerations of a Piezoelectric Actuator,* in *ICASE*2000, Insitute for Computer Applications in Science and Engineering: Hampton, VA. p. 1-6.

33. Incropera, F.P. and D.P. Dewitt, *Fundamentals of Heat and Mass Transfer*. 5 ed2002, New York: John Wiley & Sons. 981.

34. Churchill, S.W. and R. Usagi, *A General Expression for the Correlation of Rates of Transfer and Other Phenomena.* AIChE Journal, 2004. **18**(6): p. 1121-1128.